

Premixed and non-premixed generated manifolds in large-eddy simulation of Sandia flame D and F

Preprint; published in Combustion & Flame 153, 394-416 (2008)

A.W. Vreman^{1,2,3}, B.A. Albrecht¹, J.A. van Oijen¹,
L.P.H. de Goey¹ and R.J.M. Bastiaans^{1,4}

¹ Combustion Technology, Department of Mechanical Engineering, Technische Universiteit Eindhoven, Den Dolech 2, 5600 MB Eindhoven, The Netherlands

² Vreman Research, Godfried Bomansstraat 46, 7552 NT Hengelo The Netherlands

Abstract

Premixed and non-premixed flamelet generated manifolds have been constructed and applied to large-eddy simulation of the piloted partially premixed turbulent flames Sandia Flame D and F. In both manifolds the chemistry is parametrized as a function of the mixture fraction and a progress variable. Compared to standard non-premixed flamelets, premixed flamelets cover a much larger part of the reaction domain. Comparison of the results for the two manifolds with experimental data of flame D show that both manifolds yield predictions of comparable accuracy for the mean temperature, mixture fraction and a number of chemical species, like CO₂. However, the non-premixed manifold outperforms the premixed manifold for other chemical species, the most notable ones being CO and H₂. If the mixture is rich, CO and H₂ in a premixed flamelet are larger than in a non-premixed flamelet, for a given value of the progress variable. Simulations have been performed for two different grids to address the effect of the large-eddy filter width. The inclusion of modeled subgrid variances of mixture fraction and progress variable as additional entries to the manifold have only small effects on the simulations of both flames. An exception is the prediction of NO, which (through an extra transport equation) was found to be much closer to experimental results when modeled subgrid variances were included. The results obtained for flame D are satisfactory, but despite the unsteadiness of the LES, the extinction measured in flame F is not properly captured. The latter finding suggests that the extinction in flame F mainly occurs at scales smaller than those resolved by the simulation. With the presumed β -pdf approach significant extinction does not occur, unless the scalar subgrid variances are overestimated. A thickened flame model, which maps unresolved small-scale dynamics upon resolved scales, is able to predict the experimentally observed extinction to some extent.

³Electronic mail: bert@vremanresearch.nl

⁴Author to whom correspondence should be addressed; electronic mail: r.j.m.bastiaans@tue.nl.

1 Introduction

Large-Eddy Simulation (LES) of combustion as research topic has gained an increasing amount of attention in recent years (see reviews [1, 2]). The subject is complicated, because questions regarding LES methodology and modeling issues related to chemistry need to be considered simultaneously.

In order to be able to perform three-dimensional time-dependent simulations of turbulent flows with combustion, it is usually not realistic to solve transport equations for all species occurring in the chemical reaction process. Therefore, it is common to apply a reduction technique to limit the number of transport equations that need to be carried in 3D. One group of reduction techniques are formed by the flamelet approaches (see e.g. Peters [3]). In these approaches the detailed, multidimensional chemistry is mapped to one or a few representative variables, such that the dimension of the chemistry is reduced to the small number of representative variables. The mapping functions are represented by a one- or multidimensional table, constructed from a set of flamelets. Each flamelet corresponds to a one-dimensional simulation with detailed chemistry.

The mixture fraction Z is the most important representative variable in non-premixed combustion. In general the mixture fraction is solved by a transport equation. To include effects of the finite time of the chemical reactions (non-equilibrium chemistry), we need an additional representative variable, for which the scalar dissipation rate is the classic choice [3, 4, 5]. In turbulent computations, the scalar dissipation rate, which is essentially the square gradient of Z , can usually not be resolved, and then the quantity is modeled (algebraically in most cases). Another complication is that steady non-premixed flamelets parametrized by the scalar dissipation rate do not fill the complete range from equilibrium chemistry to complete extinction. To let simulations access the entire reaction range nevertheless, the database of non-premixed flamelets needs to be modified by, for example, incorporation of unsteadiness [5], inclusion of finite flamelet domains with non-vanishing fluxes at the end points [6], or interpolation (present paper).

A different reduction method is the mixture fraction/progress variable approach, which in the context of LES has been used by Pierce & Moin [6]. In this approach the scalar dissipation rate is abandoned as representative variable, and a progress variable, describing the local progress of the chemical reaction, is introduced instead. The progress variable is a suitable linear combination of appropriate chemical species, and it is solved by its own transport equation, unlike the scalar dissipation rate in the classic approach.

The progress variable is a natural choice to describe the progress of the entire chemical reaction towards chemical equilibrium. The mixture fraction/progress variable approach is an efficient reduction technique, since only two additional transport equations need to be solved, while in principle, without much additional cost, all chemical species can be retrieved from the flamelet table. When the chemistry represented by the table is a good model, and the simulation is able to predict both mixture fraction and progress variable accurately, accurate predictions of all chemical species can be expected.

Although Pierce & Moin [6] used non-premixed flamelets only, the mixture fraction/progress variable approach can be based on premixed flamelets as well [7, 8, 9, 10, 11]. In contrast, the mixture fraction/scalar dissipation rate approach can not be based on premixed flamelets, since premixed flamelets have a scalar dissipation rate of zero. With the applications of premixed and partially premixed problems in mind, it seems useful to investigate LES with the mixture fraction/progress variable approach also for premixed flamelets. Therefore, the purpose of this paper is to investigate and compare the behavior of both premixed and non-premixed flamelet databases in LES with the mixture fraction/progress variable approach.

Since in practice, non-premixed and premixed combustion may occur in the same flow, it is important to know the practical limits of a given approach. The premixed flamelet approach is able to predict premixed and also some partially-premixed problems quite well [10, 11], but

can it be used in LES of partially premixed or non-premixed applications? If the latter were the case, the approach would be applicable to a wide range of combustion problems. This question has been addressed earlier: premixed flamelets were used to compute non-premixed burning rates successfully [12], and the mixture fraction/progress variable approach based upon premixed flamelets was used to test laminar non-premixed and partially premixed flames [13, 14]. The premixed flamelet approach has also been applied in Reynolds averaged Navier-Stokes simulations (RANS) of Sandia Flame D,E and F [15]. The experiments of these turbulent partially premixed jet flames (supported by premixed pilot flames) have been well documented [16, 17, 18]. Apart from the jet Reynolds number the conditions of these flames are the same; the Reynolds number for flame F (49000) is twice as high as in flame D, and for flame E it is in between.

In the present work, the premixed flamelet approach will be tested further, now for large-eddy simulation of Sandia Flame D and F. For other numerical studies of the Sandia flames, LES or RANS, the reader is referred to Refs. [5, 19, 20, 21, 22] for simulations using flamelet methods and to Refs. [23, 24, 25, 26] for simulations using transported PDF methods. Because of the severe extinction observed in Flame F, this flame is quite a challenge for LES, and to our knowledge large-eddy simulations of Sandia Flame F have not been reported in literature before. Although this work is first of all about Flame D, a number of results for flame F have been included to demarcate more clearly abilities and limits of specific modeling approaches. Since LES resolves more scales than RANS, the modeling of small scales may be more general and results are hopefully less sensitive to modeling details. However, we will see that in LES of turbulent combustion extra complications arise, in particular when non-standard reaction effects like extinction occur at unresolved scales, like in LES of flame F.

Five sections will follow. In the next section we will present the LES methodology, the two flamelet approaches, and the specification of the flow configuration of the test-case. Section 3 serves to illustrate several issues related to the LES methodology (all based on flame D): the effects of grid resolution and inflow boundary conditions, the role of the subgrid model and the explicit density filter, influence of including scalar subgrid variance or thickened flame modeling, and the technique of NO prediction. Having established and tested the methodology, we will then present more extensive results for the premixed simulations and compare them to non-premixed results for Sandia Flame D in section 4. Results for Sandia Flame F will be presented in section 5. Finally, the conclusions will be summarized in section 6.

2 Approach

The presentation of the approach is in five parts: formulation of the filtered equations (subsection 2.1), the description of the premixed and non-premixed flamelet databases (subsection 2.2), specification of the numerical method (subsection 2.3), specification of models for subgrid chemistry (subsection 2.4), and the numerical formulation of the test-cases (subsection 2.5).

2.1 The large-eddy equations

The Navier-Stokes equations with parametrized chemistry considered in the present paper read:

$$\frac{\partial \rho}{\partial t} + \frac{\partial \rho u_j}{\partial x_j} = 0, \quad (1)$$

$$\frac{\partial \rho u_i}{\partial t} + \frac{\partial \rho u_i u_j}{\partial x_j} = -\frac{\partial p}{\partial x_i} + 2\frac{\partial \mu S_{ij}}{\partial x_j}, \quad (2)$$

$$\frac{\partial \rho Z}{\partial t} + \frac{\partial \rho u_j Z}{\partial x_j} = \frac{\partial}{\partial x_j} \left(\rho D_Z \frac{\partial Z}{\partial x_j} \right), \quad (3)$$

$$\frac{\partial \rho Y}{\partial t} + \frac{\partial \rho u_j Y}{\partial x_j} = \frac{\partial}{\partial x_j} \left(\rho D_Y \frac{\partial Y}{\partial x_j} \right) + \omega_Y, \quad (4)$$

$$\rho = f_1(Z, Y), \quad (5)$$

$$T = f_2(Z, Y), \quad (6)$$

$$\omega_Y = f_3(Z, Y), \quad (7)$$

where the summation convention over repeated indices is used, while ρ , \mathbf{u} , p , T , Z and Y represent density, velocity vector, pressure, temperature, mixture fraction and progress variable respectively. The functions f_j are used to define the quantities that are retrieved from a flamelet database. In the next subsection we will clarify that T is related to ρ by the combustion approximation, the equation of state specified in the next subsection. When all the variables in that equation of state are tabulated as functions of Z and Y , the temperature is also known as a function of Z and Y . The mixture fraction Z is a conserved scalar, whereas the progress variable is a (linear) combination of reaction product species:

$$Y = Y_{\text{H}_2}/M_{\text{H}_2} + Y_{\text{H}_2\text{O}}/M_{\text{H}_2\text{O}} + Y_{\text{CO}_2}/M_{\text{CO}_2}, \quad (8)$$

where Y_i and M_i represent the mass fraction and the molar mass of species i , respectively. This progress variable has been chosen since its behavior is monotonic for each premixed flamelet. Note that the equation for Y is not conservative, since it contains the source term ω_Y , which is a linear combination of other source terms, analogous to Eq. (8). In addition the rate of strain is defined by

$$S_{ij} = \frac{1}{2} \left(\frac{\partial u_i}{\partial x_j} + \frac{\partial u_j}{\partial x_i} - \frac{2}{3} \frac{\partial u_k}{\partial x_k} \delta_{ij} \right), \quad (9)$$

while the viscosity μ is a function of temperature according to Sutherland's three-coefficient law. We assume Lewis numbers of unity for all species, which is common practice in turbulent combustion [5, 27]. This implies that ρD_Z and ρD_Y are the same and equal to

$$\lambda/c_p = 2.58 \cdot 10^{-5} (T/298 \text{ K})^{0.69} \text{ kg m}^{-1} \text{ s}^{-1}, \quad (10)$$

where λ is the thermal conductivity and c_p the specific heat [28].

The LES formulation starts from the filtered Navier-Stokes equations. The filter is denoted with an overbar and is associated with the length-scale Δ (the filter-width), which is taken equal to h , the local mesh-size. For the velocity components the common Favre-average is used, $\tilde{u}_i = \overline{\rho u_i}/\bar{\rho}$. A straightforward formulation for combustion is obtained if subgrid terms arising from the nonlinearities in μ , D_Z , D_Y , f_1 , f_2 and f_3 are neglected and commutation between filter and derivatives is assumed. The closure problem of the convective terms in momentum and scalar equations is treated with an eddy-viscosity μ_t specified later on, and an eddy-diffusivity μ_t/Sc_t . Thus the approximated filtered equations become:

$$\frac{\partial \bar{\rho}}{\partial t} + \frac{\partial \bar{\rho} \tilde{u}_j}{\partial x_j} = 0, \quad (11)$$

$$\frac{\partial \bar{\rho} \tilde{u}_i}{\partial t} + \frac{\partial \bar{\rho} \tilde{u}_i \tilde{u}_j}{\partial x_j} = -\frac{\partial \bar{p}}{\partial x_i} + 2 \frac{\partial (\mu + \mu_t) \tilde{S}_{ij}}{\partial x_j}, \quad (12)$$

$$\frac{\partial \bar{\rho} \tilde{Z}}{\partial t} + \frac{\partial \bar{\rho} \tilde{u}_j \tilde{Z}}{\partial x_j} = \frac{\partial}{\partial x_j} \left((\bar{\rho} D_Z + \frac{\mu_t}{Sc_t}) \frac{\partial \tilde{Z}}{\partial x_j} \right), \quad (13)$$

$$\frac{\partial \bar{\rho} \tilde{Y}}{\partial t} + \frac{\partial \bar{\rho} \tilde{u}_j \tilde{Y}}{\partial x_j} = \frac{\partial}{\partial x_j} \left((\bar{\rho} D_Y + \frac{\mu_t}{Sc_t}) \frac{\partial \tilde{Y}}{\partial x_j} \right) + \bar{\omega}_Y, \quad (14)$$

$$\bar{\rho} = f_1(\tilde{Z}, \tilde{Y}), \quad (15)$$

$$\bar{T} = f_2(\tilde{Z}, \tilde{Y}), \quad (16)$$

$$\bar{\omega}_Y = f_3(\tilde{Z}, \tilde{Y}). \quad (17)$$

We remark that μ , D_Z , D_Y , and f_i in the approximate filtered equations are expressed in filtered quantities only, thereby ignoring the subgrid closure problem caused by these nonlinear functions. However, we will compare our results with results from computations where

the functions f_i also depend on the subgrid variances of Z and Y (section 4). For the present flows, the effects of including subgrid scalar variances (based on presumed β -pdf modeling) will appear to be quite limited.

The eddy-viscosity model that we use was proposed in [29] and reads

$$\mu_t = \hat{p}C \left(\frac{\beta_{11}\beta_{22} - \beta_{12}^2 + \beta_{11}\beta_{33} - \beta_{13}^2 + \beta_{22}\beta_{33} - \beta_{23}^2}{\alpha_{kl}\alpha_{kl}} \right)^{1/2}. \quad (18)$$

Here the model constant $C = 2.5C_S^2$ is related to the Smagorinsky constant, $C_S = 0.1$. The tensor β equals the gradient model,

$$\beta_{ij} = \Delta_k^2 \alpha_{ki} \alpha_{kj}, \quad \alpha_{ki} = \frac{\partial \tilde{u}_i}{\partial x_k}, \quad (19)$$

where Δ_k is the filter-width (grid-spacing) in direction x_k . A priori tests have shown that the gradient model [30] mimics the structure of the exact turbulent stress quite accurately [31]. Since straightforward use of the gradient model causes stability problems, the gradient model was recast into the eddy-viscosity formulation above. Model (18) has shown to be as accurate as the dynamic subgrid model [32] in wall-bounded and free shear flow and, like the dynamic model and the wall-adapted local eddy-viscosity model [33], the present model vanishes near walls and in transitional flow. Unlike the other models (18) also vanishes in one-dimensional expanding flow (stretched flamelets), which can be a desirable property in LES of combustion [34]. In fact the expression exactly vanishes for certain types of laminar flow, the same types of flow for which the exact incompressible subgrid dissipation is zero [29]. For the eddy-diffusivity we adopt a constant value of $Sc_t = 0.4$, a value commonly used in LES-combustion studies [5, 20].

2.2 Flamelet generated manifolds

In this subsection we describe how the chemical parametrization, expressed by the functions or manifolds f_i introduced in the previous section, is obtained. The manifolds are built from a set of flamelets, each one of them corresponding to a different mixture fraction. A flamelet is the solution of a low Mach number formulation of the one-dimensional Navier-Stokes equations supplemented with detailed chemistry. The detailed chemistry model presently employed is the GRI 3.0 reaction scheme. In this paper we use two different databases, one built of steady premixed flamelets, the other built of steady non-premixed flamelets.

The premixed and non-premixed flamelets presently considered are both solutions of the following one-dimensional equations for N species:

$$(\rho u)' = -\rho K, \quad (20)$$

$$(\rho u Y_i)' - (\rho D_i Y_i')' = -\rho K Y_i + \omega_i, \quad (21)$$

$$(\rho u H)' - (\rho D_H H')' = -\rho K H + \left(\sum_{i=1}^N (\rho D_i - \rho D_H) H_i Y_i' \right)', \quad (22)$$

$$(\rho u Z)' - (\rho D_Z Z')' = -\rho K Z, \quad (23)$$

$$(\rho u K)' - (\rho \mu K')' = -2\rho K^2 + \rho_{\text{ox}} a^2, \quad (24)$$

$$\frac{1}{\rho} = \frac{RT}{p_0} \sum_{i=1}^N \frac{Y_i}{M_i}, \quad (25)$$

$$H = \sum_{i=1}^N Y_i H_i \quad \text{with} \quad H_i = H_i^0 + \int_{T^0}^T (c_p)_i dT, \quad (26)$$

where the symbol H represents the enthalpy, and K is the flame stretch rate. Equation (25) represents the combustion approximation, in which p^0 is the ambient pressure. The diffusion

	Fuel	Oxidizer
Y_{CH_4}	0.156	0.000
Y_{O_2}	0.196	0.233
Y_{N_2}	0.647	0.767
T [K]	294	291
H [J/g]	-732.1	-7.1

Table 1: Fuel and oxidizer compositions

coefficients ρD_H , ρD_Z and ρD_i are all the same and equal to Eq. (10). Other symbols are (or will become) clear in their context. Only in this section the prime denotes the derivative of a one-dimensional function. Although zero in the present case, the preferential diffusion terms are included in (22) for completeness of the formulation.

Non-premixed and premixed flamelets mainly differ because of the boundary conditions imposed to equations (20-24). In a non-premixed flamelet fuel enters at one side

$$Y_i(-\infty) = Y_i^{\text{fu}}, \quad H(-\infty) = H^{\text{fu}}, \quad Z(-\infty) = 1, \quad K'(-\infty) = 0, \quad (27)$$

and oxidizer enters at the other side

$$Y_i(\infty) = Y_i^{\text{ox}}, \quad H(\infty) = H^{\text{ox}}, \quad Z(\infty) = 0, \quad K(\infty) = a, \quad (28)$$

The values used at the fuel and oxidizer side are specified in Table 1. The translational degree of freedom of the non-premixed flamelet equations is removed by choosing the stagnation point at $x = 0$: $u(0) = 0$. The parameter that determines a single non-premixed flamelet is the strain rate a applied at the oxidizer side. To construct a non-premixed manifold, flamelets are computed for a range of strain rates. The function $Z(x)$ is monotonic for each non-premixed flamelet.

In a premixed flamelet, fuel and oxidizer enter at the same side, which is expressed by Dirichlet boundary conditions at the inlet:

$$Y_i(-\infty) = Z^m Y_i^{\text{fu}} + (1 - Z^m) Y_i^{\text{ox}}, \quad (29)$$

$$H(-\infty) = Z^m H^{\text{fu}} + (1 - Z^m) H^{\text{ox}}, \quad (30)$$

$$Z(-\infty) = Z^m, \quad (31)$$

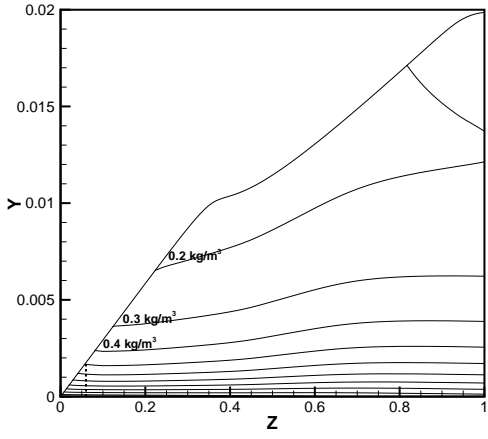
$$K(-\infty) = 0. \quad (32)$$

Neumann boundary conditions are imposed at the outlet:

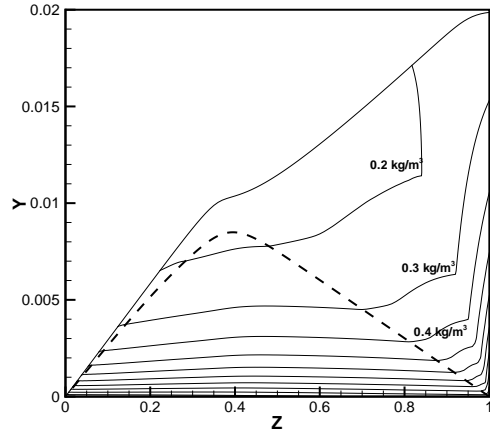
$$Y_i'(\infty) = 0, \quad H'(\infty) = 0, \quad Z'(\infty) = 0, \quad K'(\infty) = 0. \quad (33)$$

The translational degree of freedom is removed by choosing a fixed reference temperature at $x = 0$. The parameter of this system is the stoichiometry of the fresh mixture denoted by the mixture fraction Z^m . Note that $Z(x) = Z^m$ and $K(x) = 0$. Therefore, $\rho u = \rho_u s_L$ is constant with ρ_u the density of the unburnt mixture at $-\infty$ and s_L the laminar burning velocity. To construct the premixed manifold, premixed flamelets have been computed for $Z^m=0.06, \dots, 1$ (stepsize 0.01). The progress variable Y , defined by equation (8), is monotonic for each premixed flamelet.

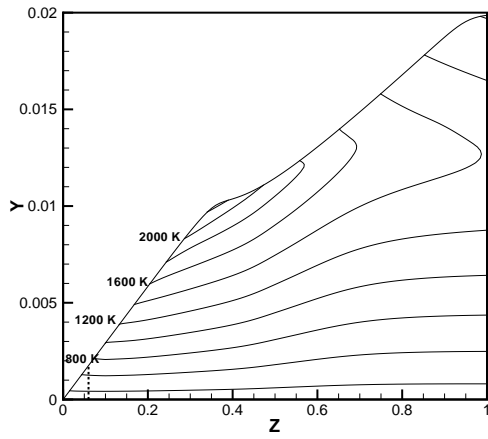
The premixed and non-premixed manifolds, which result from the one-dimensional flamelet calculations and which serve as input for the 3D simulations, are shown in Fig. 1. The figure visualizes the functions f_2 and f_3 , which prescribe the temperature and source-term ω_Y , respectively. Density manifolds are not shown since according to the flamelet equations density is proportional to the reciprocal of the temperature (combustion approximation). The flamelet



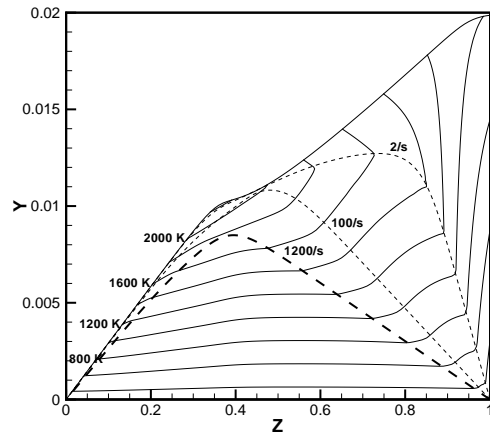
(a)



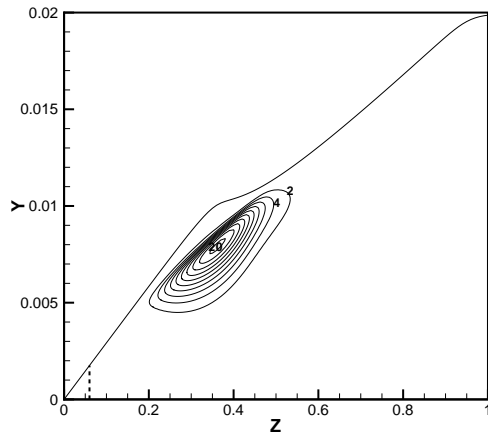
(b)



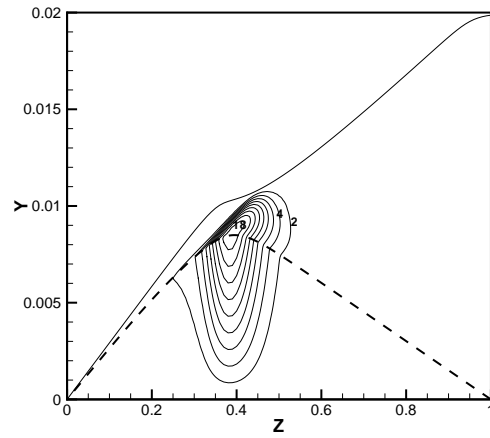
(c)



(d)



(e)



(f)

Figure 1: Premixed (left) and non-premixed manifolds (right) for density ρ (function f_1), temperature T (function f_2) and source term ω_Y (function f_3). The contour increment is 0.1kg/m^3 for the density manifolds (top), 200K for the temperature (middle), and $2\text{kg}/(\text{m}^3\text{s})$ for the source term of the progress variable (bottom). The dashed line in the premixed manifolds represents the premixed flamelet for $Z = 0.06$; left from that line steady premixed flamelets do not exist. The bold dashed line in the non-premixed manifolds represents the non-premixed flamelet for $a = 1200/s$; below that line steady non-premixed flamelets do not exist. The thin dashed lines in (d) represent the non-premixed flamelets corresponding to $a = 100/s$ and $a = 2/s$.

corresponding to the maximum value ($a = 1200/\text{s}$) of computed non-premixed flamelets is close to the region of extinction, where steady non-premixed flamelets do not exist (see Fig. 1bdf). A linear interpolation scheme was used to fill the manifold between the (Z, Y) curve represented by the flamelet corresponding to the maximum value of a and the horizontal axis $Y = 0$. The steady non-premixed flamelet equations do not cover that region. It is obvious that the interpolation is an ad-hoc solution to fill the non-equilibrium part of the reaction domain, and Fig. 1 shows clearly that it introduces some non-smoothness in the non-premixed manifold. In fact, the premixed flamelets do not cover the entire reaction zone either; steady premixed flamelets could not be obtained for $Z < 0.06$, and the corresponding region in the premixed manifold was also filled by linear interpolation. However, the region where steady flamelets do not exist is not only much smaller in the premixed case than in the non-premixed case, it is also a region with no activity of the source term of the progress variable (ω_Y). In contrast, the edge of the regime of steady non-premixed flamelets cuts off a large part of the non-equilibrium chemistry (large activity of ω_Y). After interpolation, the resolution of the manifolds is 101 points in the Z -direction, equally spaced between 0 and 1, and also 101 points in the Y -direction, equally spaced between 0 and Y_{max} . Here Y_{max} is a function of Z . Bilinear interpolation is used when this manifold is accessed in the large-eddy simulations to return values of f_i for the local values of Z and Y .

2.3 Numerical discretization

We use a straightforward and efficient implementation to solve the equations (11-17) numerically. The approach involves a Poisson equation for the pressure, like the methods presented by Pitsch & Steiner [5], and Pierce & Moin [6]. For the continuity and momentum equations the standard finite volume method is employed, with second-order central differencing on a staggered Cartesian mesh. Thus the discrete convective terms would conserve kinetic energy if the density were constant. The scalar equations have been recast into the equivalent advective (non-conservative) formulations. To the latter Van Leer's third-order accurate MUSCL scheme, which is TVD, is applied. For the temporal discretization the explicit Euler method is used, except for the convective terms in the momentum equations, which are treated with Adams-Bashforth. One case was run with a second-order two-stage Runge-Kutta method with pressure correction at each stage, and the results were quite similar (see section 3.2).

After calculation of convective and viscous terms, the scalars and (uncorrected) velocities are updated to the new time level. Then the density, temperature and source terms at the new time level are calculated using the flamelet table with entries Z and Y and bilinear interpolation. Afterwards the density is filtered, with a $2h$ top-hat filter as discussed hereafter.

Once the density at the new time level is known, the continuity equation provides the divergence of the momentum vector at the new time level. Application of the divergence operator to the momentum equation leads to the Poisson equation for the pressure:

$$\frac{\partial^2(p\delta t)}{\partial x_i^2} = \frac{\rho^{n+1} - \rho^n}{\delta t} + \frac{\partial w_i}{\partial x_i}, \quad (34)$$

where δt is the time-step and \mathbf{w} is the updated momentum vector before pressure correction. The Poisson equation is iteratively solved with multigrid and SOR relaxation, and then the momentum vector is corrected with $-\nabla p$ multiplied with δt .

Fig. 1b shows that the dependence of density to Z and Y can be quite stiff ($\rho \sim 1/T$); $\partial\rho/\partial Y$ ($\partial\rho/\partial Z$) is relatively large close to the line $Y = 0$ ($Z = 1$). If the progress variable increases from zero to for example 0.0015 (20% of its maximum value), the density reduces with more than a factor 2. As a result small fluctuations in the mixture fraction and progress variable can cause relatively large density oscillations [19], which, through the pressure correction, may induce unrealistically large values of velocity fluctuations and destabilize the simulation. Thus the density gradients may be larger than the numerical method can handle, in particular if the

smallest resolved scales in Z and Y are of the size of the grid-spacing. Since the latter is the case in LES, a procedure to control these fluctuations is recommended.

Control of density oscillations in large-eddy simulation can be achieved by removing the smallest resolved scales in the scalar fields Z and Y by explicit filter operations [19]. In this work we adopt a similar approach, but instead of explicitly filtering the scalars Z and Y , we filter the density itself to obtain a better resolution of the density gradients. Thus the explicit filter is not applied before, but after the retrievals from the flamelet database. In more detail, the explicit density filter used in the present LES means that each $\bar{\rho}$ that occurs in the left-hand side of equations (11) to (14) is replaced by

$$\hat{\rho} = f_1(\widehat{\tilde{Z}}, \widehat{\tilde{Y}}), \quad (35)$$

where the 'hat' denotes the explicit filter operation. The explicit filter used in this paper is the three-dimensional top-hat filter with width $2h$, where h is the local mesh-spacing. The explicit density filter can be interpreted as the incorporation of correction terms to Eq. (11-14) proportional to $\hat{\rho} - \bar{\rho}$. Using Taylor expansions of the top-hat filter it is readily shown that these correction terms are of the order of $O(h^2)$, comparable to the order of the discretization method. Like the discretization error, the density correction terms vanish if the mesh-spacing approaches zero. The implementation of the filter uses three one-dimensional filters, subsequently applied for each direction. Each one dimensional filter is an average across three grid-points using the weights $\frac{1}{4}$, $\frac{1}{2}$ and $\frac{1}{4}$ (approximation of the top-hat filter with the trapezoidal rule). This filter is not conservative on a non-uniform grid, but we verified that for the present grids, a conservative filter leads to very similar results (see section 3.2).

We only apply the explicit filter to the density and not to the temperature and source-term parametrizations, since the continuity requirement causes the solution to be much more sensitive to numerical errors in $\bar{\rho}$ than to numerical errors in \tilde{T} and $\bar{\omega}_Y$. Therefore, no explicit filter is used for the latter quantities, in order to represent these with as much as detail as possible on the available mesh.

2.4 Subgrid chemistry

The modeling of the subgrid turbulence has been specified in subsection 2.1. In this subsection we address the modeling of subgrid chemistry effects, that is how the subgrid terms arising from the filtered nonlinear functions f_i can be treated. Here we consider two approaches appearing in literature of LES of turbulent combustion: the presumed β -pdf approach and the thickened flame approach.

In the presumed β -pdf approach the two-dimensional database is extended to a database of dimension four ($101 \times 101 \times 21 \times 21$), spanned by the four entries Z , $\text{var}(Z)$, Y and $\text{var}(Y)$. The range of each variance is discretized using 21 points, non-uniformly distributed between 0 and the theoretical maximum, $Z(1 - Z)$ for the mixture fraction. The variance levels are quadratically clustered near zero, such that the spacing varies between 0.25% and 10% of the maximum variance. The values in the manifold for non-zero variances were calculated using probability density functions with a so-called beta-distribution [36, 37], assuming statistical independence of Z and scaled Y (Y scaled with its Z -dependent maximum Y_{max}).

The following variance models are presently adopted,

$$b\Delta_k^2(\partial_k \tilde{Z})^2 \quad \text{and} \quad b\Delta_k^2(\partial_k \tilde{Y})^2, \quad (36)$$

where $b = 1$ is a reasonable choice (see section 5). These expressions are slightly different from standard models for the variances due to the incorporation of grid anisotropy through Δ_k (compare Ref. [29]). The inclusion of anisotropy directly follows from the Taylor expansions by which such kind of models can be derived. The variance models are similar to the gradient model for the turbulent stresses [30].

In the presumed β -pdf approach, the LES-filtered chemical quantities are interpreted as statistical means over subgrid scales, which are assumed to obey the β -pdf probability distribution with appropriate mean and variance. To obtain the presumed β -pdf manifolds in practice, one applies weighted averagings in Y and Z space, for a collection of weight functions of β -function shape. Because of the averaging, the β -pdf method reduces the source terms, and thus it deals with the flame thickening imposed by the LES. Another issue is flame wrinkling, which increases the turbulent burning velocity. Assuming that the flame wrinkling goes down to the smallest turbulent motions, LES has to deal with subgrid wrinkling effects. In principle the β -pdf approach takes the subgrid wrinkling into account, as can be concluded from excellent predictions in DNS computations, where very likely some of the wrinkling was subgrid [36]. However, these predictions were only excellent when the *exact* subgrid variance of a single scalar was used. In actual LES we need to model the subgrid variance, and, in case multiple scalars are used, statistical independency or another assumption is also required.

An alternative way to deal with subgrid flame effects is the thickened flame approach. In contrast to the presumed β -pdf approach, only source terms are modified in the thickened flame approach. Thickened flame modeling (Colin *et al.* [34]) relies on a mathematical invariance of the equations: if viscosity and diffusivities are multiplied with a constant factor F , and if the algebraic source terms are divided by F , then the solution of the equations does not change, except for the length-scale and time-scale, which should be multiplied with F [38]. This invariance is quite general: it holds for the three-dimensional time-dependent equations, provided all source terms are algebraic functions of the flow variables. In principle, turbulent flows satisfy the invariance as well. However, it is important to recognize that the invariance itself does not allow for more efficient computations, since the ratio between largest and smallest length-scale in the flow is not altered by the thickening transformation. For more efficient computations, the scaling transformation has to be restricted to specific mechanisms in the flow, and thus problems arise. For example, one wishes to increase the length-scale of the combustion, but not the length-scale of the external geometry and the turbulent velocity field. In such case the thickening transformation is applied to combustion scales only, and then the transformation needs to be supplemented by a model (a model for subgrid flame wrinkling in thickened flame LES, for example).

The thickened flame concept has been adopted fruitfully in LES of premixed turbulent combustion [34, 39], but also non-premixed applications have been considered [42]. It is remarked that the mathematical scaling invariance is general and thus applies to both premixed and non-premixed combustion. In the non-premixed case, the flamelet depends on the strain-rate, which is divided by F as well (this implies that the thickened strain-rate can be represented on the mesh and can be related to the resolved strain-rate in LES). It has also been argued that spatial and temporal variations of the thickening factor F are allowed [42].

The thickened flame approach in LES includes subgrid wrinkling of the flame through the efficiency factor E [39, 40]: the molecular diffusion is multiplied with EF , while the source term is multiplied with E/F . The model for E requires the physical flame thickness as input parameter. In general the thickness of the flame varies in space and therefore it needs to be modeled. However, the bounds for E are independent of flame thickness [34]: $1 < E < F^{2/3}$, where the lowerbound corresponds to no wrinkling and the upperbound to maximum wrinkling. In this paper we consider a very simple model for E , we model $E = F^\zeta$. We remark that the thickening factor F in LES should be interpreted as l_R/l , where l_R is the resolved LES flame thickness (related to Δ), and l the unknown local flame thickness, varying in space and time. Thus the present powerlaw efficiency model is implicitly based on the assumptions that flame wrinkling goes down to the flame thickness (which is not always true) and that the fractal dimension of the subgrid wrinkled flame surface [41] equals $2 + \zeta$. More detailed models for E in partially and non-premixed applications may be developed in the future. Having performed a number of thickened flame simulations, we propose an empirical value $\zeta = \frac{1}{2}$ for the present cases. This value is in between the bounds just mentioned and equal to the fractal coefficient

used in Ref. [39]. Results are expected to be sensitive to the particular value of ζ , in particular those of flame F, which is close to global extinction.

The original flame thickening model proposes to multiply the molecular diffusion with EF explicitly in the simulations. However, it is important to recognize that the eddy-diffusivity and numerical diffusion cause flame thickening already. Numerical diffusion of scalars is needed to keep the scalars between their physical bounds. Instead of adding more diffusion explicitly, we define the factor EF as the thickening factor introduced by the subgrid and numerical diffusion. Thus the actual F is determined from the following equation:

$$F^{3/2} = EF = \frac{D_Y + \mu_t/(\hat{\rho}Sc_t) + D_n}{D_Y}, \quad (37)$$

where

$$D_n = \frac{\sum_{i=1}^3 |u_i| h_i g_i}{2|\nabla \tilde{Y}|^2} \quad (38)$$

is the estimated numerical diffusion coefficient (we use the Y -equation; alternatively, the Z -equation can be used). Here h_i is the local grid-spacing, while the functions g_i can be estimated from the numerical 'dissipation' term in the equation for Y^2 . If in a given grid point the flow is sufficiently smooth such that the limiter function is not called, the leading-order truncation term of the MUSCL scheme prescribes $g_i = \frac{1}{6} h_i^2 (\partial^2 Y / \partial x_i^2)^2$. Note that the summation convention over repeated indices is not used here. However, in grid points where the upwind scheme does call the limiter function, we define $g_i = (\partial Y / \partial x_i)^2$, to estimate the first-order upwind dissipation introduced by the limiter. Finally, having determined the local value of F , the source-term ω_Y in the thickened flame model is multiplied with $E/F = F^{-1/2}$.

2.5 Formulation of the test-cases

In this subsection we describe the physical and numerical configuration of Sandia Flame D. The configuration of Sandia Flame F is the same with the exception of the measured inlet profiles correspond to a bulk-velocity that is two times larger than in Flame D. Sandia Flame D is a piloted coaxial methane-air flame [16]. The fuel, a mixture of 25% methane and 75% air, corresponding to $Z = 1$, leaves the inner nozzle (diameter $D = 7.2\text{mm}$) with a bulk velocity of 49.6m/s. The pilot flow (bulk-velocity 10.8m/s and mixture fraction $Z = 0.27$) exits from a wider nozzle, which is centered around the inner nozzle and has a diameter of $2.62D$. Around the outer nozzle there is a flow of air with a velocity of 0.9m/s.

The streamwise coordinate z is defined to be zero at the nozzle exit. Experimental results were measured for $z < 80D$. To reduce the effect of the outflow boundary conditions in the region of measurement the computational domain was taken considerably longer; the numerical outflow conditions were imposed at $z = 150D$. The extended length of the computational domain accounted for 20% of the number of grid-points. The computational domain was rectangular, most convenient for the Cartesian grid that we used. A cross section of the flow domain was a horizontal square with a length of about $40D$ in each direction (x and y). The cells with centers $x = y = 0$ were on the axis of the flow. The advantage of a Cartesian grid is that the explicit time-step can be larger than on cylindrical grids. The grid was stretched in all three directions and contained $128 \times 128 \times 320$ cells, with a minimum grid-spacing equal to $D/5$ in the z -direction and $D/8$ in the x and y -directions. Also results for coarser grids will be shown, this grid was approximately coarsened with a factor of 1.5 in each direction ($80 \times 80 \times 192$ cells). Outflow conditions in vertical and horizontal directions were zero normal derivatives for all variables, except for the pressure, which was maintained equal to the ambient pressure in outflow planes in the x and y -directions. The inflow conditions will be described in the next section.

The simulations were started from an initial state where all velocities and scalars were initialized to zero, except from the streamwise velocity w , which was initialized to the velocity

of the outer flow (0.9m/s). The constant time step equalled $5 \cdot 10^{-6}$ seconds. Time-averaging of statistics was started at 0.06s (larger than the flow through time on the axis until $80D$), and all simulations reported in this and the following sections were run until approximately 0.16s. However, the premixed fine-grid simulation was continued beyond 0.3s, to verify that the statistics were converged at 0.16s.

3 Modeling considerations

Before we compare the chemistry predictions for premixed and non-premixed databases, we discuss several important details: numerical resolution and inlet boundary conditions, effect of subgrid model, the role of the density filter, the effect of modeling or omitting subgrid scalar invariances, and the method by which we predict NO. All results in this section are presented for the premixed simulations only, but conclusions would most probably be the same if the non-premixed database were used.

3.1 Inlet boundary conditions and grid refinement

One of the main problems to reproduce the experimental results by simulations arises from the inlet boundary conditions. The inner nozzle in the experiment is quite narrow, while the pilot is not a simple co-flow jet, but a premixed flame ejected through a large amount of small holes. Thus some simplification of geometry seems to be inevitable before performing computations. We have chosen not to simulate the flow inside the cylinders, but to impose inflow boundary conditions using the measurements of the flow at the exit or just outside the exit. Measurement data is available for $z = 0$, which coincides with the exit, but the full profiles have also been measured at $z = D$. At $z = 0$ the mean profiles of species, and hence the mean density profile, are discontinuous near the radius of the inner nozzle wall, since the boundary layer in the inner nozzle is too thin to be resolved on the grid. However, at $z = D$, the gradients of mean density and velocity are less strong and vary more continuously on the scale of the grid. This is preferable from a numerical point of view.

Both inlet conditions $z = 0$ and $z = D$ have been tested for flame D. It is remarked that the mean velocity profiles were measured in Darmstadt [18], while the mass fractions of the species (including mixture fraction and progress variable) were measured in the Sandia laboratories. For the $z = 0$ inlet condition, the inlet mean mixture fraction and progress variable were prescribed by the measured bulk values as step-wise constant functions, while for the $z = D$ they were obtained from the measurements at $z = D$. Linear interpolation was used to obtain the values at grid points.

The simulations appear to be sensitive to the mean profiles specified. This is clearly illustrated by Fig. 2, where we compare results of simulations with the two inlet conditions described above. It appears that the mean mixture fraction on the centerline drops too early in the simulation where the inflow was specified at $z = 0$, while the mixture fraction is very well reproduced when the inflow is specified at $z = D$ (Fig. 2a). However, in the latter case the prediction of the mean velocity profile is worse than in the former case (Fig. 2b). Comparing the streamwise turbulence intensity on the centerline, we observe that the velocity fluctuations are overpredicted in the case with inflow at $z = 0$. Apparently, the strong gradients in the mean profiles cause too large velocity fluctuations in this case. Hence the turbulence is stronger than in the case with inflow at $z = D$, reason why the onset of the decay of mean velocity and mixture fraction on the centerline occurs at an earlier point. Since for the testing of different flamelet models it is essential that the mixture fraction (and progress variable) are predicted accurately, the results with inflow boundary condition $z = D$ are most suitable for the further investigations in the present paper.

The sensitivity of the results to this variation of the inlet condition is not likely to be an effect of grid resolution, since we validated the simulations by grid refinement. For both inlet

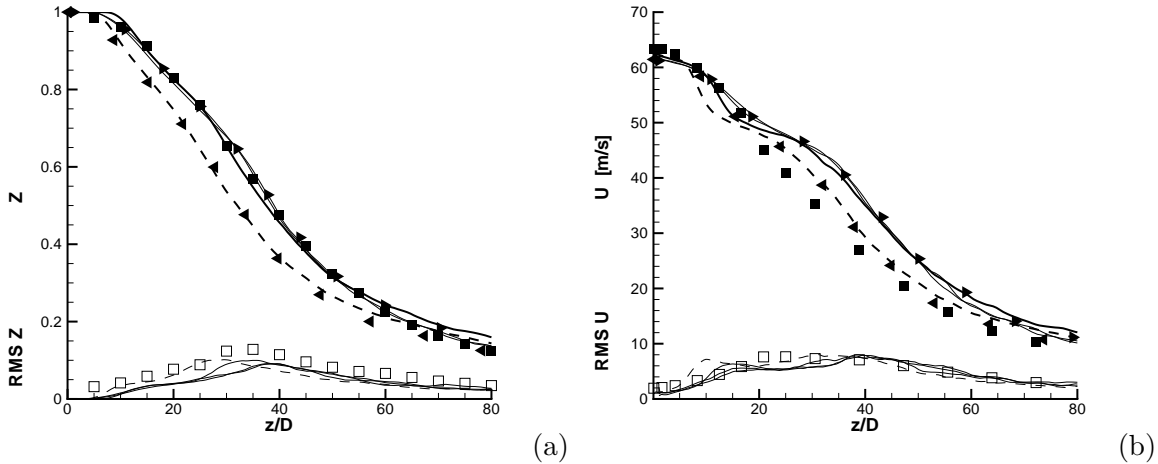


Figure 2: Flame D. Axial profiles of mean and fluctuation of mixture fraction (a) and streamwise velocity (b) obtained with premixed database. Comparison of inflow conditions and resolution. The case with the inflow boundary at $z = D$ is denoted by the solid line (fine grid) or right triangles (coarse grid). The case with the inflow boundary at $z = 0$ is denoted by the dashed line (fine grid) or left triangles (coarse grid). The additional solid lines show the effect of a larger and a smaller inlet velocity perturbation, corresponding to twice and half the reference perturbation value, respectively. The experimental data from literature [16, 18] is denoted by square symbols.

conditions, the mean centerline profiles for the fine grid appear to be almost on top of the results for the coarse grid.

The inlet velocity components were perturbed by uniform noise with amplitude profiles equal to the corresponding measured turbulence intensities. The mixture fraction and progress variable profiles were unperturbed at the inflow boundary. A more sophisticated prescription of the inflow turbulence is unlikely to be effective, since like Pitsch & Steiner [5], we found that the simulations were not very sensitive to the velocity perturbations. This is illustrated by Fig. 2, which includes the influence of inlet perturbations for one of the coarser grid simulations. At the inflow plane the fluctuations of the velocity components are uncorrelated, but the instability of creating the turbulence is strong, such that in the shear layers, within a few gridpoints from the inlet, correlation shear stress values larger than 0.5 are encountered. It is remarked that Reynolds averaged simulations of this flow are known to be sensitive to prescription of the inflow turbulence and inflow turbulent dissipation rate in particular [43].

3.2 Illustration of miscellaneous effects: subgrid turbulence, explicit density filter and time-stepping scheme

Both the subgrid model and the explicit density filter were found to reduce the velocity fluctuations in the smallest resolved scales. Velocity fluctuations are caused by the physical instabilities of the turbulence, but also by the pressure correction. The latter strongly depends on the fluctuation of the density. We used the explicit density filter, which achieves that density gradients are better represented on the grid. In this way it controls the smallest resolved scales of the density fluctuations.

Fig. 3 illustrates the role of the subgrid model and the density filter. The importance of the subgrid model is addressed by comparing the eddy-viscosity with the molecular viscosity. Thus we see that relatively close to the nozzle exit, subgrid modeling is important, while the flow seems to be resolved quite well further downstream, since there the molecular viscosity

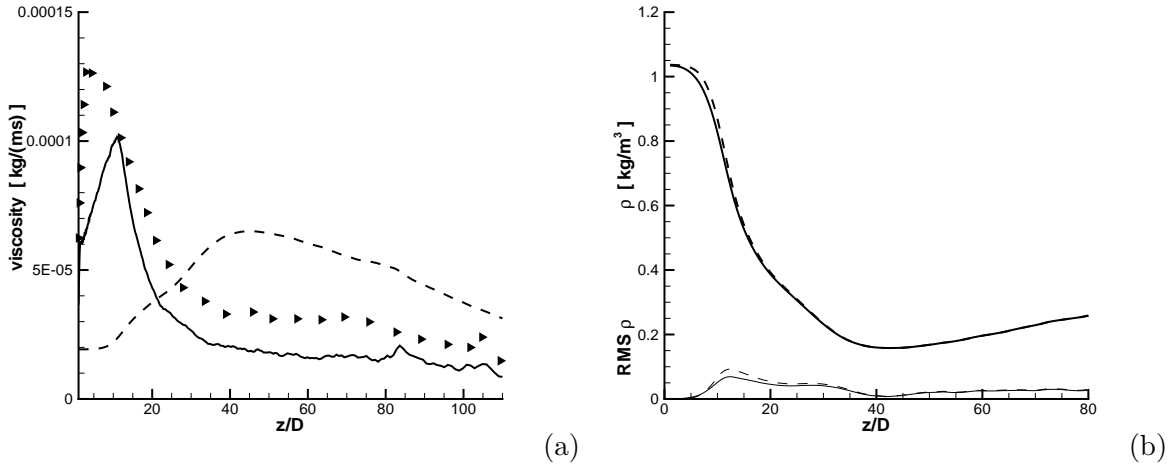


Figure 3: Flame D. (a) Eddy-viscosities (solid) and molecular viscosity (dashed) on the fine grid, and eddy-viscosity on the coarse grid (triangles); (b) mean and fluctuation of density on the centerline for the simulation with premixed flamelets: $\bar{\rho}$ as retrieved from the database before explicit filtering (dashed) and $\hat{\rho}$, the density after explicit filtering as it is passed through to the simulations (solid).

is larger than the subgrid viscosity. The eddy-viscosity of the coarse grid simulations has also been plotted; it shows that the eddy-viscosity becomes larger if the filter-width (grid-spacing) increases, as expected. Fig. 3b shows the effects of the density filter on the density itself. Here we see that the modeling, which was found to considerably affect the smallest scales, has only modest effect on the mean and root mean square of the density. That despite the small difference in $\bar{\rho}$ and $\hat{\rho}$ the density filter was found to be quite effective, illustrates that if the density is not adequately treated, oscillations on the scale of grid-spacing h may deteriorate the simulations, even when these oscillations are small.

A straightforward non-conservative implementation of the density filter (section 2.3) was used for the results throughout this paper, but a conservative three-points filter was also tested. In this test, performed on the coarse mesh, we used the three-points conservative filter (with central weight $\frac{1}{2}$), derived in Ref. [44]. Fig. 4 shows that the results are quite similar for both density filters.

As indicated in subsection 2.3 one (coarse-grid) simulation was performed with the second-order two-stage Runge-Kutta method, using the same time-step as the hybrid Adams-Bashforth Euler method. The results for the two different temporal discretizations are also compared in Fig. 4. According to the figure, the two different temporal discretizations lead to approximately the same results.

3.3 Influence of subgrid chemistry for flame D

Before we proceed with the results in the next section, we show some results to address the effect of subgrid chemistry in case of flame D. Figure 5 demonstrates that the effects are not large, on the coarse grid. Effects are very likely to be even smaller on the fine grid. For the presumed pdf-approach a similar finding has been reported before, for LES in two dimensions [45].

The progress variable is more sensitive to the subgrid chemistry than the mixture fraction. With the β -pdf model the results are somewhat worse (since due to this model ω_Y in the region close to equilibrium increases if the (small) subgrid variance increases, see section 5). With the thickened flame model the results are slightly better than without subgrid chemistry.

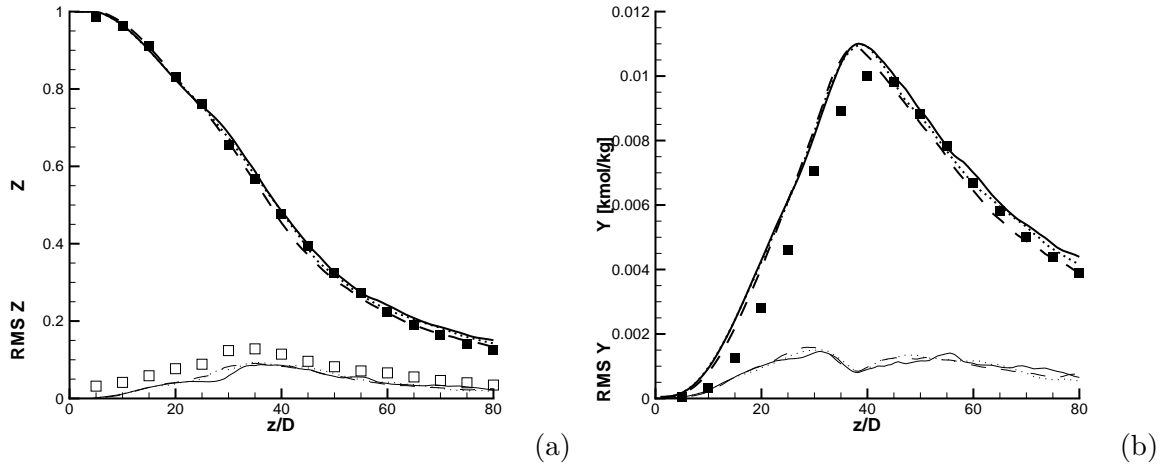


Figure 4: Flame D. Premixed simulation results on the coarse mesh. Standard case with non-conservative density filter and hybrid Adams-Bashforth Euler time-stepping (solid), compared with a simulation with the conservative density filter (dotted) and a simulation with Runge-Kutta time-stepping (dashed). Mean and fluctuation of mixture fraction (a) and progress variable (b) on the central axis. The experimental data from literature [16] is denoted with symbols.

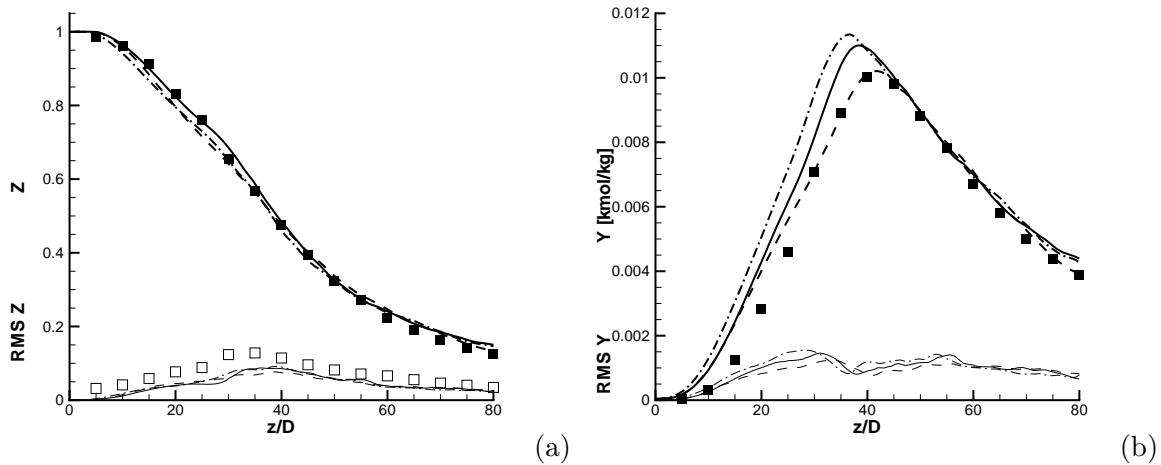


Figure 5: Flame D. Premixed coarse grid simulation results. Mixture fraction (a) and progress variable (b) on the centerline, means (bold) and fluctuations. Case without subgrid chemistry (solid) compared to presumed β -pdf (dash-dotted) and thickened flame model (dashed). The experimental data from literature [16] is denoted with symbols.

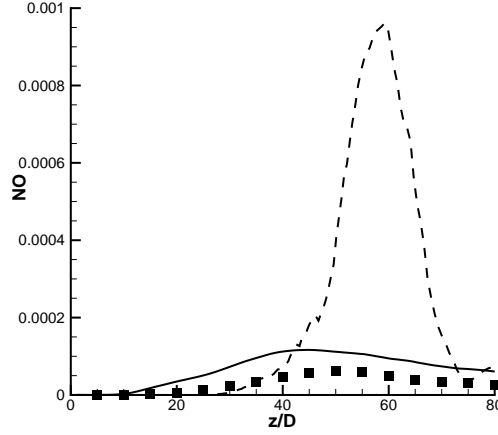


Figure 6: Flame D. Axial mean profiles of NO mass fraction, obtained directly from the manifold (dashed) or by a separate transport equation (solid). The experimental data from literature [16] is denoted with symbols.

Since the effect of these models was found to be small even for coarse grids, we present most results in section 4 on flame D for two fine grid simulations which neglected the subgrid chemistry. However, the issue of subgrid chemistry turns out to be much more important for flame F (see section 5). It is remarked that with or without subgrid chemistry, the eddy-viscosity specified in subsection 2.1 was switched on in all simulations presented in this paper.

3.4 A transport equation for NO

Since the formation of NO is known to be a very slow process, the mass fraction of NO can not properly be mapped on the range of the progress variable: the mass fraction of NO is approximately zero in the reaction domain, except for a very thin region at the upper edge of the manifold. Consequently, when NO is directly evaluated from the manifold, the computational prediction and the experimental values are completely out of range for the premixed simulation on the fine grid (Fig. 6). For a non-premixed manifold or a β -pdf subgrid closure the results are even more out of range (not shown). The NO manifolds have been inspected and they turn out to be zero everywhere except for a very thin zone near maximum Y (around $Z = 0.35$). In this thin zone NO is very large. Thus a small overprediction of Y may cause a huge overprediction of NO.

Much better predictions for NO, also shown in Fig. 6, and later on in Fig. 12, are obtained when a third scalar transport equation is added, a transport equation for the mass fraction of NO (Y_{NO}):

$$\frac{\partial \bar{\rho} \tilde{Y}_{\text{NO}}}{\partial t} + \frac{\partial \bar{\rho} \tilde{u}_j \tilde{Y}_{\text{NO}}}{\partial x_j} = \frac{\partial}{\partial x_j} \left((\bar{\rho} D_Y + \frac{\mu_t}{Sc_t}) \frac{\partial \tilde{Y}_{\text{NO}}}{\partial x_j} \right) + \bar{\omega}_{\text{NO}}, \quad (39)$$

where ω_{NO} denotes the source term. It is a function of \tilde{Z} and \tilde{Y} , and it is retrieved from the manifolds. Unlike the mass fraction of NO, the variation of the source term of NO extends over a significant part of the manifold. Note that the transport equation is of the same form as the equation for the progress variable (14). Equation (39) was not mentioned in section 2, because it is passive; it only modifies the concentration of NO; other variables are not affected.

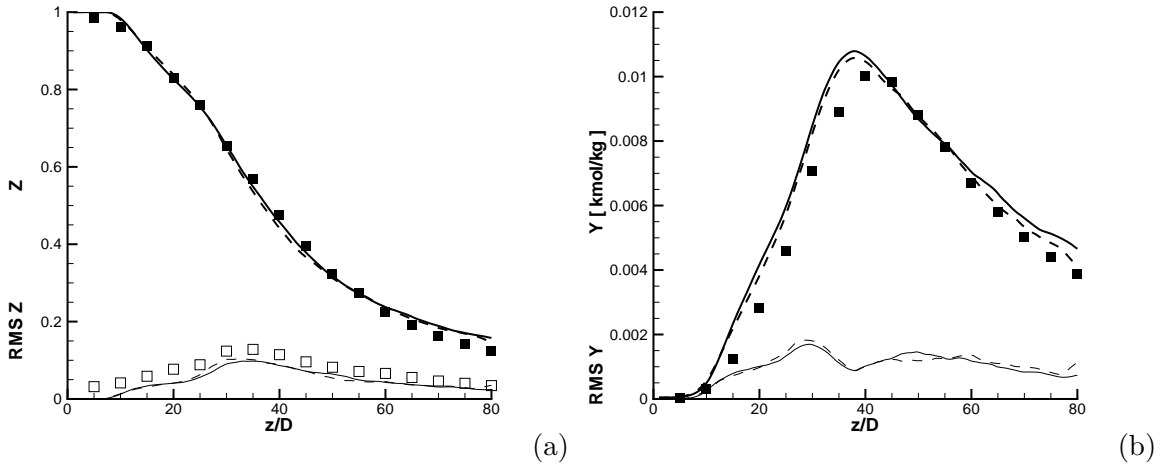


Figure 7: Flame D. Simulation results obtained with the premixed (solid lines) and the non-premixed flamelet database (dashed lines). Mean and fluctuation of mixture fraction (a) and progress variable (b) on the central axis. Bold lines represent mean values, thin lines the fluctuation. The experimental data from literature [16] is denoted with symbols.

4 Results for premixed versus non-premixed LES of flame D

In this section we compare the results of two large-eddy simulations: one with the premixed database and another with the non-premixed database. Both cases were simulated on the fine grid without subgrid variances. The minor influence of subgrid chemistry for flame D was shown in the previous subsection. In this section we focus on the differences between non-premixed and premixed results. To distinguish between these effects more clearly, the figures do not include the coarser runs with subgrid chemistry, except when mentioned otherwise. We will show statistical results for the mixture fraction and progress variable first. It is essential to obtain these quantities with accuracy, since in the present flamelet approaches the entire chemistry depends on these two quantities.

Figure 7 shows mean and fluctuation of the mixture fraction and progress variable on the centerline. In both premixed and non-premixed case the mean mixture fraction is very close to the experimental values. The progress variable is somewhat overpredicted on the rich side of the flame. The overprediction is slightly larger for the premixed case, probably because the source term of Y in the premixed manifold is about 10% higher (Fig. 8, and compare Fig. 1ef). Fig. 8 shows that the fluctuation of the source term is large compared to the mean value. This may suggest that the source term is relatively small. However, the source term is not negligible, which was confirmed by a simulation without source term, showing significant differences. Thus, the activity of the source-term indicates a small, but significant deviation from chemical equilibrium in this flame, since in chemical equilibrium the source term would be zero.

Radial profiles for mixture fraction and progress variable are shown in Fig. 9 for four different axial locations and in general they support the conclusions just drawn from Fig. 7. So we conclude that premixed and non-premixed manifolds lead to very similar and acceptable predictions of the mixture fraction and progress variable. Having verified that the predictions of mixture fraction and progress variable are reasonably accurate, we turn to the presentation of quantities that are directly retrieved from the manifold (except from NO). Firstly, we will consider the temperature and then the chemical species.

The simulated temperature in the simulations overpredicts the measured temperature upstream of the peak location (Fig. 10). It is remarked that radiation is not included in the

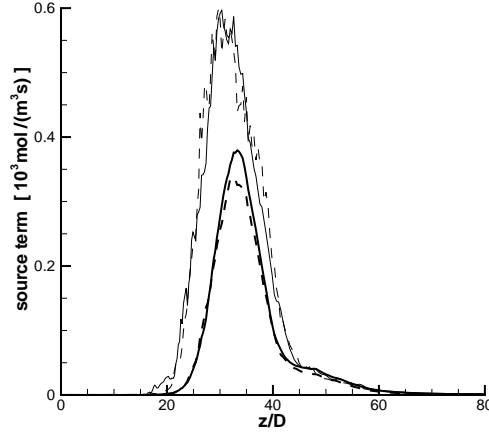


Figure 8: Flame D. Mean values of progress variable source term $\omega_Y/\hat{\rho}$ at the centerline; obtained with the premixed (solid lines) and the non-premixed flamelet database (dashed lines). Bold lines represent mean values, thin lines the fluctuation.

present flamelet models. Radiation is expected to reduce the temperature with approximately 100K, but only around the peak and further downstream. Premixed and non-premixed manifolds lead to quite similar predictions of the temperature. The fluctuation of the temperature is also predicted reasonably. Like the experimental profile, the fluctuation profiles of both simulations attain a local minimum at the location where the temperature peaks. For $z/D > 50$ the fluctuation is underpredicted, although the resolved fluctuations in LES should theoretically be somewhat lower than the experimental values.

Axial profiles for the most important chemical species in the flow are shown in Fig. 11-12. Four species which are reasonably well predicted by both simulations are shown in Fig. 11: CO_2 , H_2O , CH_4 , and O_2 . The species that are predicted less satisfactorily are shown in Fig. 12: CO , H_2 , OH , and NO . Like the temperature, the mass fractions of the species were calculated from the flamelet databases. As discussed in section 3.4, the mass fraction of NO has been solved by a separate transport equation, since it would be an order of magnitude too large otherwise. Nevertheless, the predictions shown in Fig. 12 are still considerably larger than the experimental value. This overprediction of NO is sometimes attributed to the reaction kinetics scheme GRI3.0 [35], which is known to give a larger NO mass fraction than the older scheme GRI2.11 [23]. To keep the figures more clear, the premixed coarse grid calculation results with subgrid variance model or thickened flame model have not been incorporated in the Fig. 11-12. However, an exception is made for the mass fraction of NO , which is quite important but hard to predict accurately for practical applications. This quantity becomes reasonably close to the experimental results when subgrid chemistry is accounted for (see the corresponding curves in Fig. 11d).

When observing the prediction of the chemical species, we see that the premixed profiles are almost as close to the experimental data as the non-premixed profiles, with the remarkable exception of CO and H_2 . These two species are overpredicted in both cases, but more for the premixed than for the non-premixed case. The extra overprediction in the premixed case occurs at the rich side of the flame. Since most CO_2 is formed from the intermediate CO , we would expect that higher CO would lead to lower CO_2 . Indeed, CO_2 at the rich side of the flame is relatively low for the premixed case (figure 11a, around $z = 30D$).

To investigate the overprediction of CO in more detail, we determined where the flow prefers to be in the manifolds. For this purpose we made scatter plots of all pairs (Z, Y) in a plane through the central axis at an arbitrary time (Fig. 13). Scatter plots for other times in the

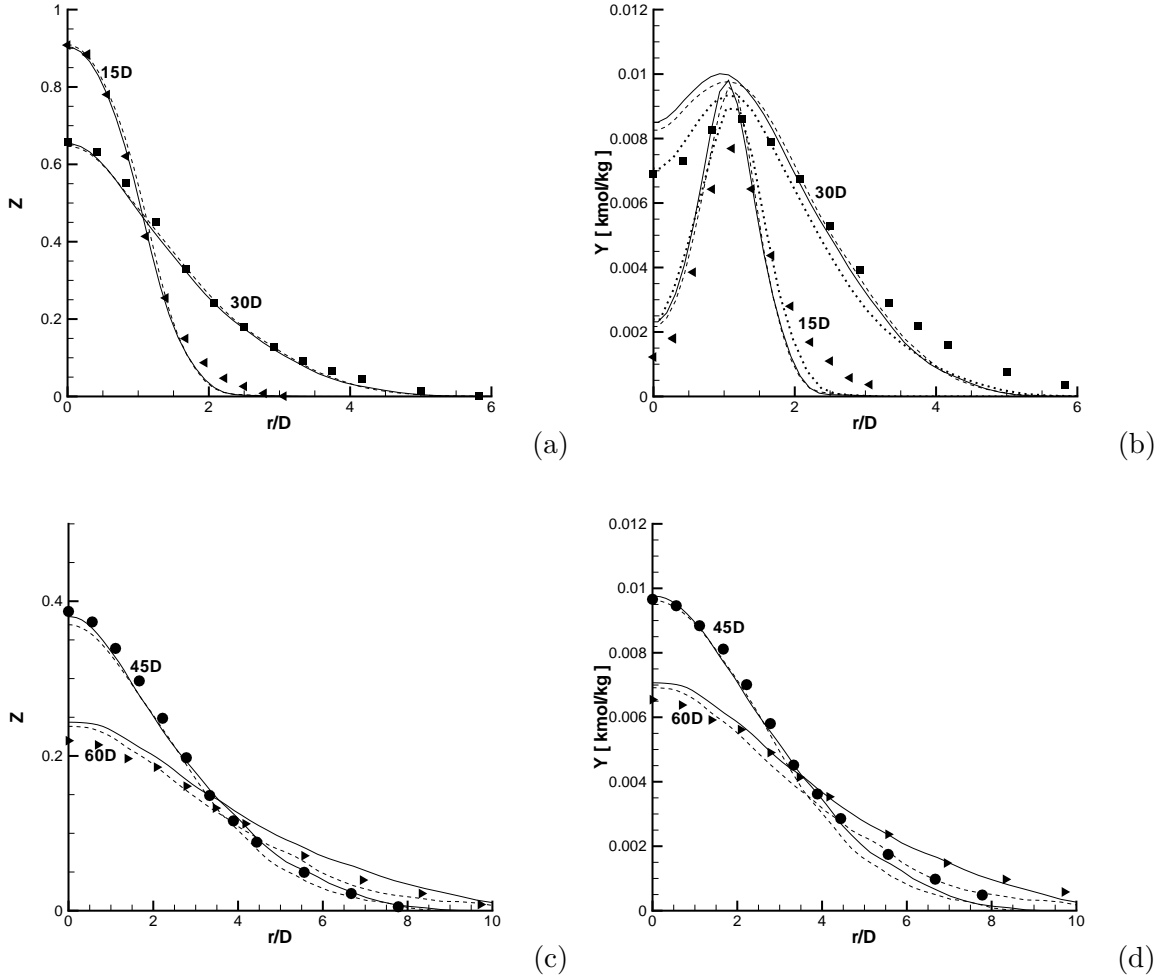


Figure 9: Flame D. Simulation results obtained with the premixed (solid lines) and the non-premixed flamelet database (dashed lines). Radial profiles of mean mixture fraction (left) and mean progress variable (right) at four different locations of the axis: $z = 15D$, $30D$ (top) and $z = 45D$, $60D$ (bottom). The experimental data from literature [16] is denoted with symbols, corresponding to the location on the z -axis: $15D$ (left-pointing triangles), $30D$ (squares), $45D$ (circles) and $60D$ (right-pointing triangles). Fig. (b) also contains results for the coarse grid thickened flame simulation (dotted).

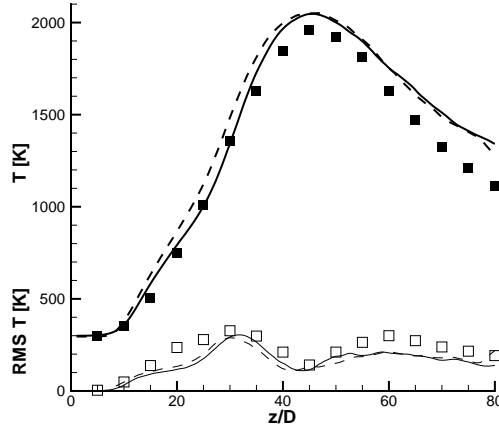


Figure 10: Flame D. Simulation results obtained with the premixed (solid lines) and the non-premixed flamelet database (dashed lines). Mean and fluctuation of temperature on the central axis. Bold lines represent mean values, thin lines the fluctuation. The experimental data from literature [16] is denoted with symbols.

statistically stationary regime were verified to be very similar to those shown. Fig. 13 shows the scatter plots on top of the manifolds for CO. It appears that the scatter points between $Z = 0.5$ and $Z = 0.7$ form a region where the CO mass fraction contour level in the premixed case is considerably larger than in the non-premixed case (0.08 versus 0.06). [A similar analysis can be made for H_2]. Fig. 13 indicates that an important reason for the different predictions of CO is the relatively high level of CO in premixed one-dimensional calculations with detailed chemistry. For values of the mixture fraction between 0.5 and 0.7, there might be less O-radicals available to form CO_2 if the flame modeled by detailed chemistry is premixed, compared to when the flame is non-premixed.

The present findings are consistent with the work of Fiorina *et al.* [13], who analyzed the ability of premixed flamelets (FPI or FGM) to predict several types of laminar diffusion flames. They found excellent agreement between premixed and non-premixed flamelets when the rich flammability limit was not exceeded, and reasonable agreement when the rich flammability limit was slightly exceeded. If we neglect the pilot, flame D (and F) can be regarded as a partially premixed rich jet flame, with an equivalence ratio outside the rich flammability limit. However, the present inlet mixture fraction is only about 1.5 times the rich flammability limit, and on the whole we do not observe very large differences between our premixed and non-premixed LES. For the corresponding equivalence ratio, the deviations between premixed and non-premixed 1D simulations turned out to be reasonably small as well (see Fig. 4 in [13]).

5 Large-eddy simulation of Sandia Flame F

Flame F has the same configuration and fuel composition as flame D, but the inlet bulk velocity is twice as high. Since a large amount of extinction was found in the measurements of this flame, this flame is regarded as a more difficult test-case than flame D. The simulations of flame F, discussed in this section, used the same grids, physical parameters and numerical methods as the simulations of flame D. The only differences were the time-step (divided by two), the time interval of averaging (start and end point of averaging were also divided by two), and the inlet conditions. Like in flame D, inlet conditions at $z = D$ were based from the measurements of species in the Sandia laboratories, and from the Darmstadt measurements of mean velocity

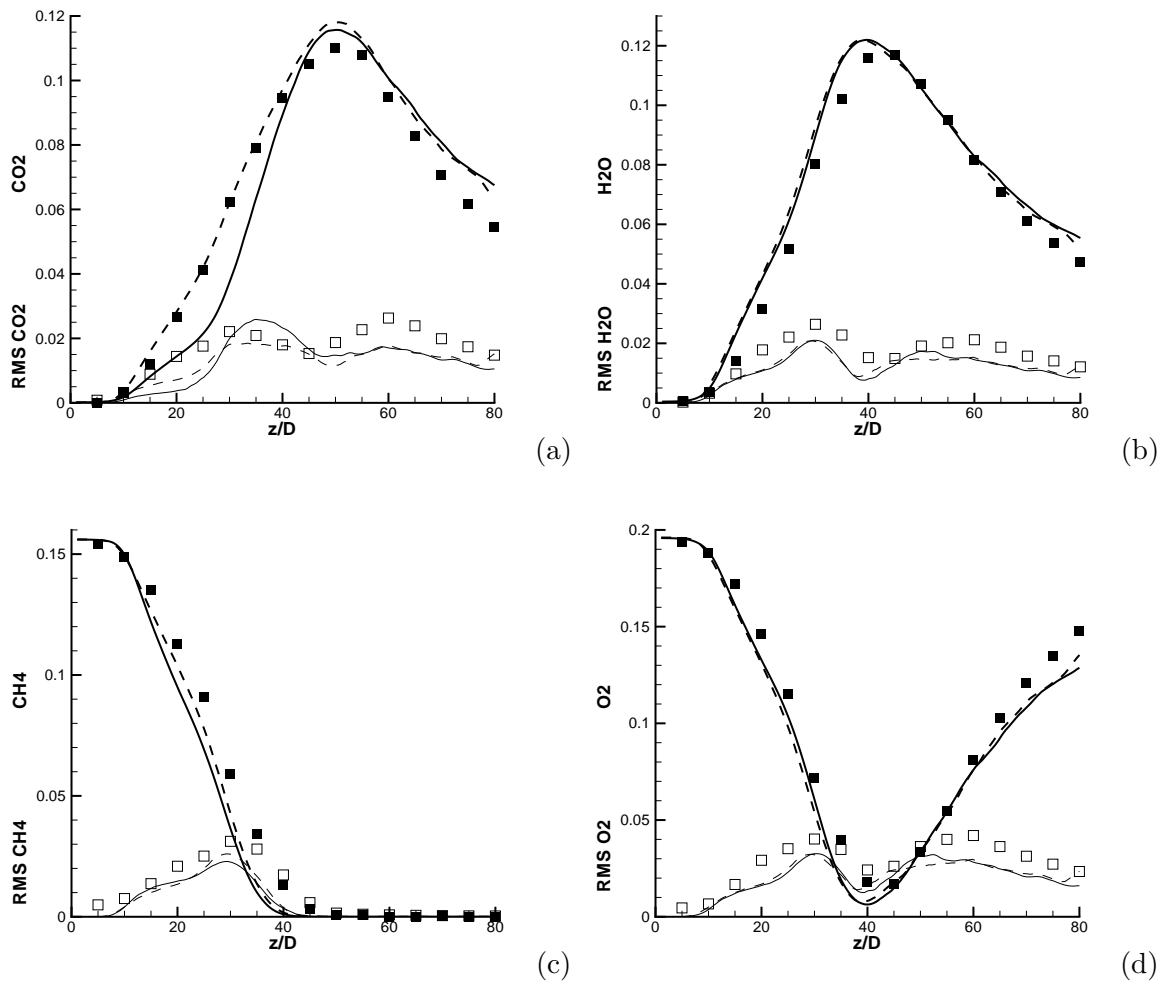


Figure 11: Flame D. Simulation results obtained with the premixed (solid lines) and the non-premixed flamelet database (dashed lines). Mean and fluctuation of mass fractions of CO₂ (a), H₂O (b), CH₄ (c) and O₂ (d) on the central axis. Bold lines represent mean values, thin lines the fluctuation. The experimental data from literature [16] is denoted with symbols.

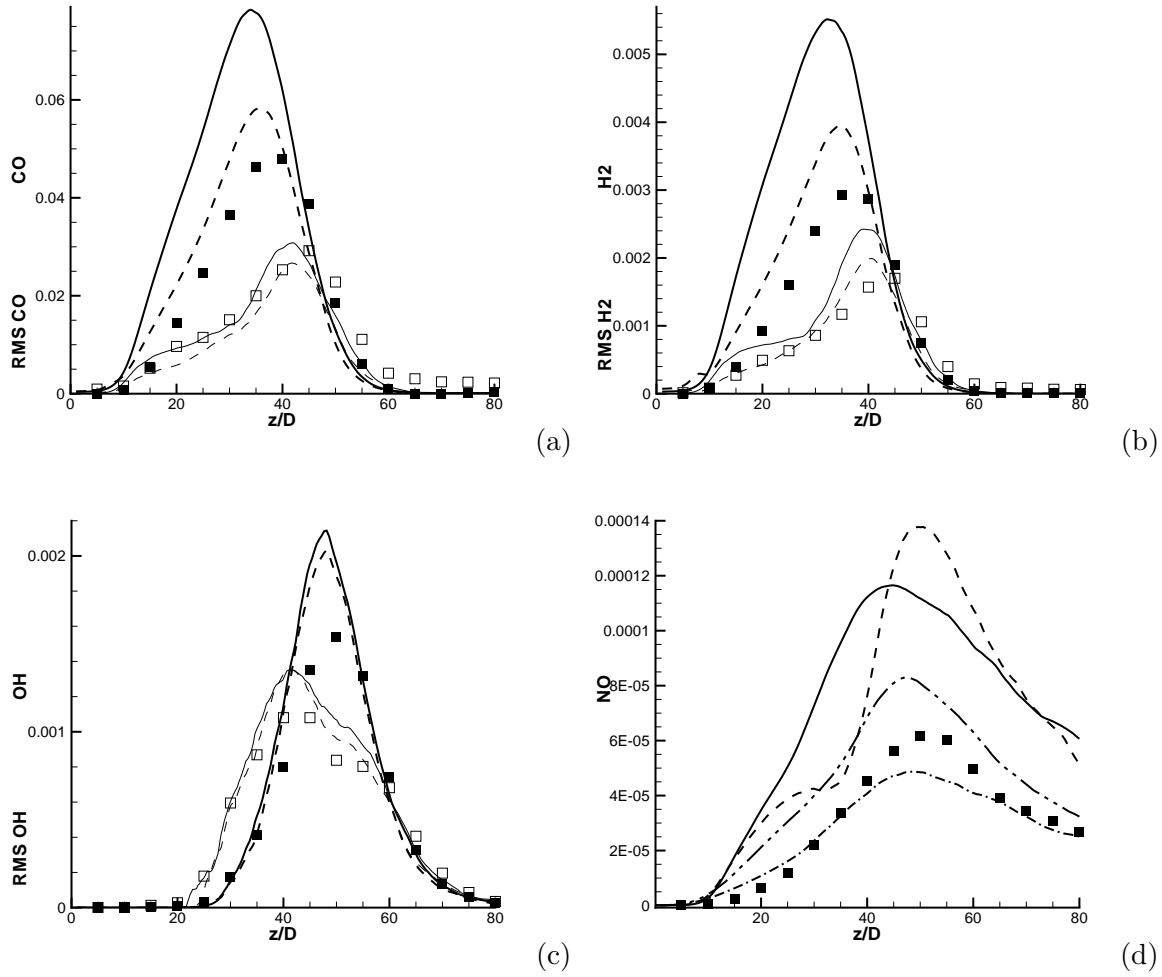


Figure 12: Flame D. Simulation results obtained with the premixed (solid lines) and the non-premixed flamelet database (dashed lines). Mean and fluctuation of mass fractions of CO (a), H₂ (b), OH (c) and NO (d) on the central axis. Bold lines represent mean values, thin lines the fluctuation. Fig. (d) also includes the premixed (coarse grid) simulations with scalar subgrid variance (dash-dotted) and with thickened flame model (dash-dot-dot). The experimental data from literature [16] is denoted with symbols.

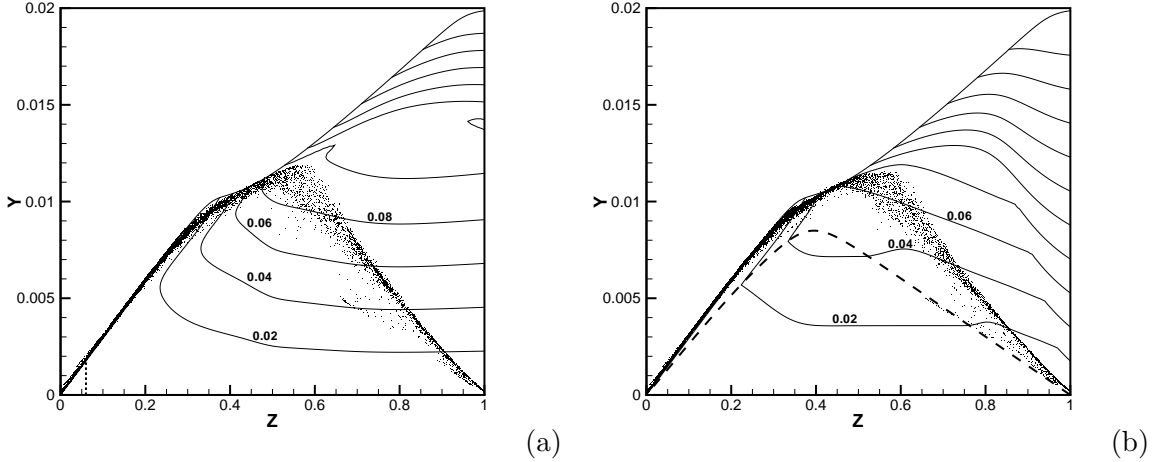


Figure 13: Premixed (a) and non-premixed manifold (b) for the mass fraction of CO. The contour increment equals 0.02. On top of the manifolds scatter plots obtained from the corresponding large-eddy simulations have been drawn (flame D). The bold dashed line in (b) represents the non-premixed flamelet for $a = 1200/s$; below that line the manifold is theoretically undefined.

profile and turbulent intensities.

The extinction as experimentally observed in this flame, was largest for the station $z/D \approx 15$. For $z/D = 15$ the radial profiles of the mixture fraction and progress variable are shown in Fig. 14. All the simulations shown in this figure used the premixed database and the eddy-viscosity / diffusivity was always switched on. The case without subgrid chemistry modeling was performed on the fine and coarse grid, and the results for the two different grids look very similar (Fig. 14). Compared to the experimental results, the two simulations without subgrid chemistry adequately predict the mixture fraction profile (Fig. 14a), but the progress variable is much too high (Fig. 14b). When the mean progress variable is plotted against the mixture fraction (Fig. 14), we see that without subgrid chemistry modeling, there is no extinction in the simulations, since the curves lie considerably above the non-premixed flamelet extinction curve ($a = 1200/s$).

Fig. 14 also includes results for coarse grid simulation with modeling of the scalar subgrid variances. The inclusion of subgrid variances does not predict extinction, at least not if the coefficient b has a reasonable value ($b = 1$). That this value is reasonable is indicated by the r.m.s. mixture fraction curves shown in Fig. 14. Both curves are from the simulation with scalar subgrid variances. The lower one shows the r.m.s. based on the resolved mixture fraction, while the other curve estimated the physical r.m.s. by the root of the sum of the resolved mixture fraction variance and the modeled mixture fraction variance. The latter result is close to the experimental data indicating that $b = 1$ is an appropriate value, at least around $z/D = 15$ (at the centerline and for $z/D > 15$ a larger value of b may be justified, see Fig. 15a, where the fluctuation of Z after correction with the subgrid variance is still relatively low). It is remarked that the value $b = 1$ is larger than what we would expect, and also larger than values that have sometimes been used. In fact the Taylor expansion for the subgrid variance models suggests $b = 1/12$, but it is known that a similar model for turbulent stresses underpredicts the magnitude of the turbulent stresses if the coefficient is $1/12$. [31]. A constant coefficient of $b = 0.1$ for the subgrid scalar variance models has been suggested by others [25, 46]. We also tested a dynamic procedure to obtain the coefficient b in flame F, and then we found typically values between 0.1 and 0.2. Thus the dynamic model and the Taylor estimate are out of range, perhaps because the actual scalar fields are relatively smooth, due to the TVD scheme.

To illustrate that the β -pdf approach does predict extinction when the scalar subgrid vari-

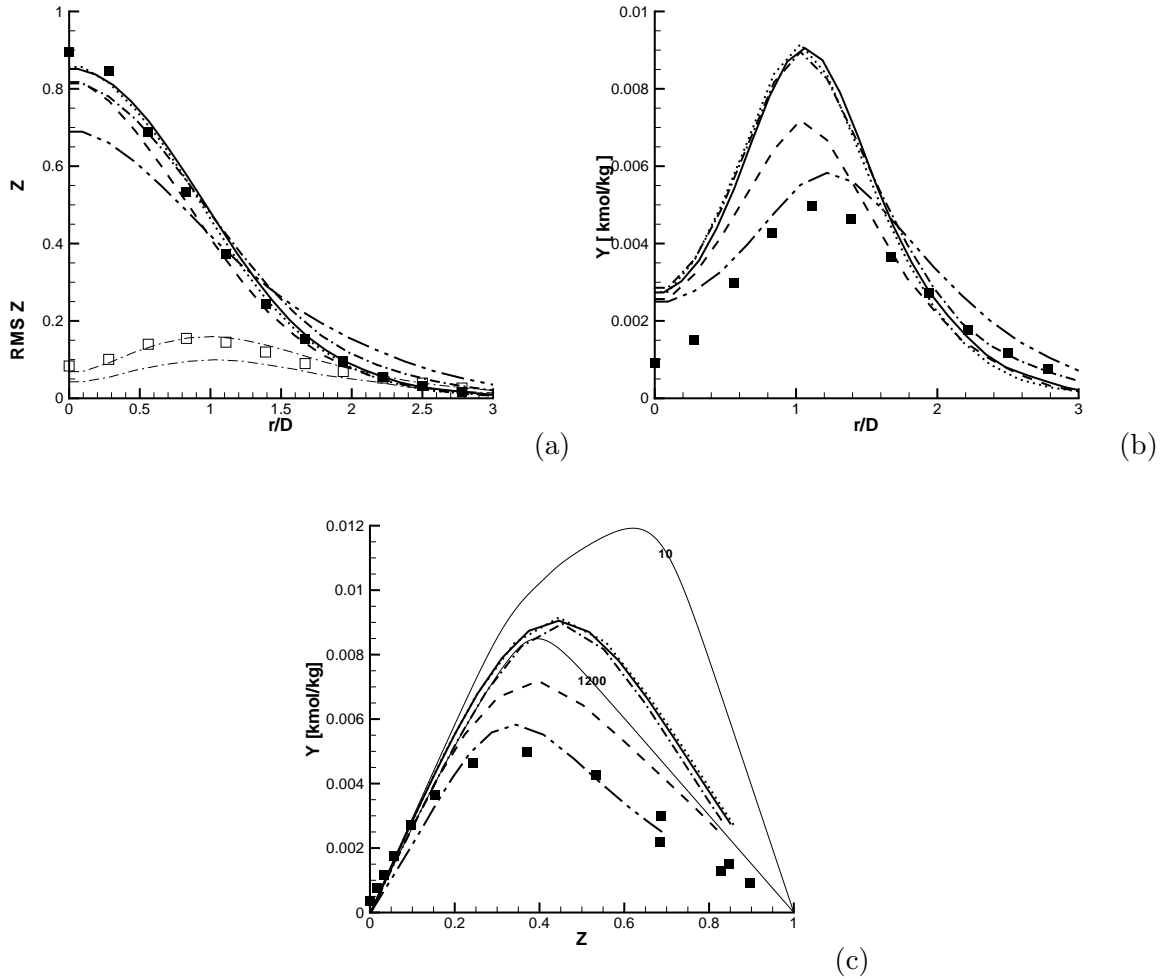


Figure 14: Flame F. Premixed simulation results. Radial profiles at $z/D = 15$. Mixture fraction (a) and progress variable (b) in physical space, and progress variable in mixture fraction space (c). Five simulations: without subgrid chemistry (fine grid (solid) and coarse grid (dotted)); with subgrid variance model, $b = 1$ (dash-dotted) and $b = 4$ (dash-dot-dot); with thickened flame model (dashed). Experimental data [16] is denoted with symbols. The thin dash-dotted lines in Fig. (a) represent the mixture fraction fluctuation for case $b = 1$: resolved fluctuations (lower curve) and the root of resolved plus subgrid variance (higher curve). Fig. (c) also contains the non-premixed flamelet curves for $a = 10/s$ and $a = 1200/s$ (the latter one is very close to extinction).

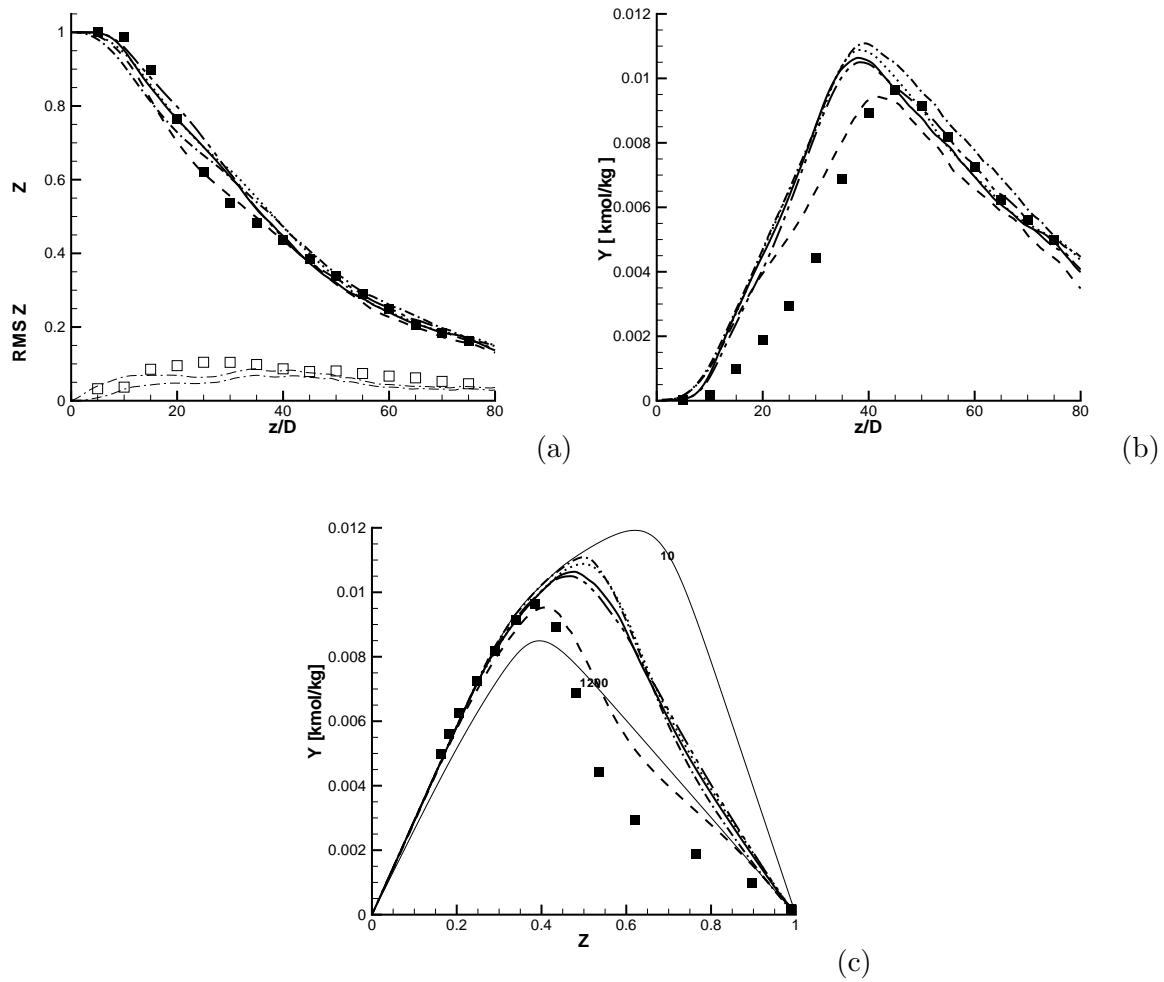


Figure 15: Flame F. Axial profiles for premixed and non-premixed cases. Caption as in the previous figure, with the exception that in the present figure the dash-dot-dot line represents a non-premixed simulation without subgrid chemistry.

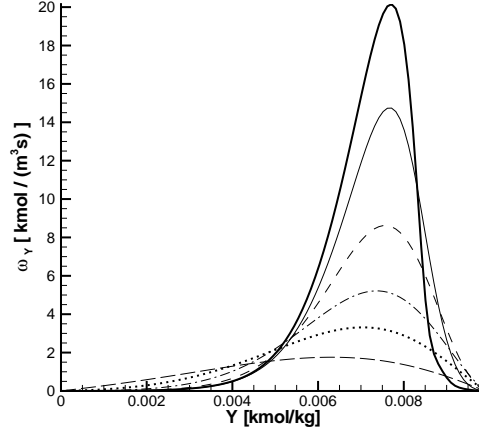


Figure 16: Curves extracted from the premixed four-dimensional manifold. Source term ω_Y against Y for stoichiometric $Z = 0.35$, with scalar subgrid variances of Z and Y equal to a fraction of the maximum tolerated values $Z(1 - Z)$ and $Y(Y_{max} - Y)$, with $Y_{max} = 0.099$. The fractional levels of the subgrid variances are: 0% (bold solid), 1% (thin solid), 4% (dashed), 9% (dash-dotted), 16% (dotted), and 30% (long dash).

ances are overestimated is shown by one curve in Fig. 14c, obtained for $b = 4$. As argued above, $b = 4$ is too large in important parts of the domain, and despite the nice prediction of extinction in mixture fraction space, the mixture fraction profile itself is clearly too flat for $b = 4$ (Fig. 14a). That the β -pdf model does not predict extinction for $b = 1$ can be caused by the choice of the presumed joint probability distribution, which is presently constructed from independent β -pdf distributions. For small subgrid scalar variances and specific manifold locations (\tilde{Z}, \tilde{Y}) the pdf-averaged source term may increase with increasing variance. This is illustrated by Fig. 16, where for the stoichiometric $Z = 0.35$ the source term ω_Y has been plotted for increasing values of the variance. Near equilibrium ($Y > 0.09$), and for variances up to 5%, the source term increases if the variance increases. For variances up to 30%, the source term remains larger than the non-averaged source term for $Y > 0.09$. This feature hinders the transition from near equilibrium to states further away from equilibrium. This explains the lack of extinction observed with the β -pdf approach for reasonable values of the subgrid variances. A probability distribution of Y which is more skewed towards equilibrium or which is conditioned on Z could cure this problem.

At present the best results are obtained with the thickened flame model, which predicts a significant amount of extinction (Fig. 14bc). Since the non-averaged manifold is premultiplied with a factor that is always smaller than one, the source term decreases with increased subgrid chemistry in the entire manifold (unlike the β -pdf approach as demonstrated by Fig. 16). The quenching caused by the thickened flame model appears to be somewhat too small (Y too high), not in the entire flow field, but around the location $z/D = 15$ in particular (compare the axial profiles in Fig. 15b, which show better predictions further downstream). We now argue why the thickened flame model predicts insufficient extinction relatively close to the inlet. The thickened flame model moves the unresolved flame dynamics (extinction in this case) to a larger scale, such that it can be resolved by the unsteady LES. Because of the thickening, the resolved stretch and scalar dissipation rate are sufficient to trigger the extinction. However, the larger flame thickness implies that the extinction process takes more time, since the time scale of the thickened equations also increases with the thickening factor F (as discussed in section 2.4). The thickening factor F implicitly induced by the present thickened flame model attains values between 15 and 35 typically. This means that the representative extinction time ($1/1200s$)

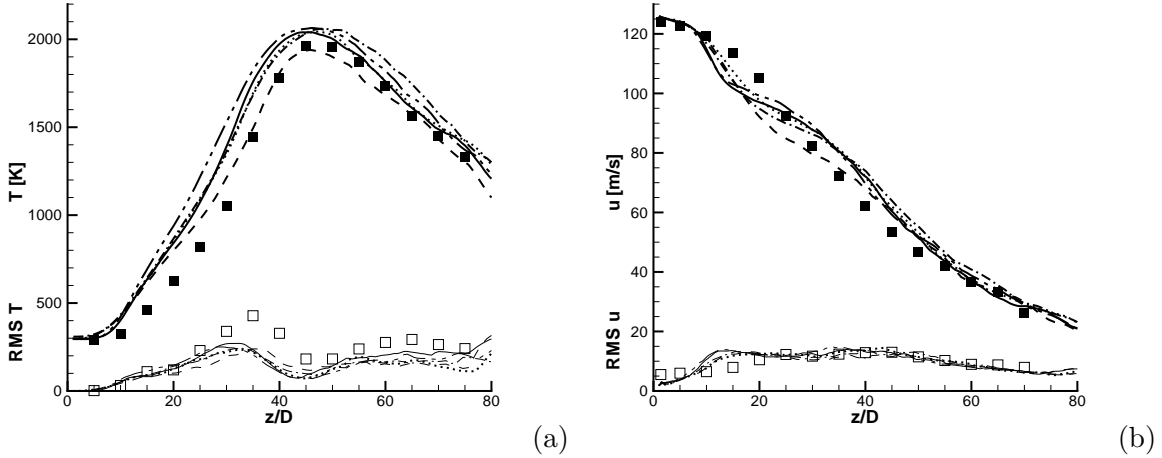


Figure 17: Flame F. Mean (bold) and fluctuation of the axial temperature (a) and streamwise velocity (b) for flame F. Four premixed simulations: without subgrid chemistry (fine grid (solid) and coarse grid (dotted)); with subgrid variance model, $b = 1$ (dash-dotted); with thickened flame model (dashed). Non-premixed simulation: without subgrid chemistry, fine grid (dash-dot-dot). The experimental data from literature [16, 18] is denoted by square symbols.

should be multiplied with F to obtain the modeled extinction time, which is therefore at least 0.01s. Using the streamwise velocity at the radial flame front (about 30m/s), we find that the thickened extinction process is not completed before $z = 0.3\text{m} \approx 40D$. This might explain the insufficient extinction predicted relatively near the inlet.

The fact that the simulations of flame F are not as successful as those of flame D could indicate that the flamelet assumptions are less valid for flame F than for flame D. First, the extinction process of a primarily non-premixed flame is modeled with a steady premixed flamelet. This problem may be less serious than it seems, since properties of non-premixed flames during extinction can be close to those of a premixed flame (see Ref. [47], p189). Second, compared to flame D, the larger Reynolds number of flame F corresponds a lower Kolmogorov scale η . If the flame thickness were the same in both flows, the flamelet assumption would have more chance to be violated in flame F, since the flamelet assumption requires that the ratio of η divided by flame thickness is sufficiently large. However, the larger strain in flame F leads to a lower flame thickness (since the flame thickness can be estimated as $(D_T/a)^{1/2}$ [47], where D_T is the thermal diffusion coefficient and a the strain rate). In case all eddies stretch the flame, a^2 is proportional to the turbulent dissipation divided by viscosity. Then the estimated flame thickness scales with η ; the ratio of flame thickness and η does not change (compared to flame D). In case the flame is stretched by large eddies only, the flame thickness does not reduce so much as η , and in that case the flamelet assumption may be less applicable.

The plots of the axial profiles (Figs. 15-18) includes results for a single simulation with the non-premixed manifold (fine grid). To limit the amount of curves in the figures, the non-premixed case was not shown in Fig. 14 (for the same reason the premixed case with subgrid variances for $b = 4$ was included in Fig. 14 only). It appears that, like the premixed case, the non-premixed simulation without subgrid chemistry stays (too) close to equilibrium and does not predict the extinction in the flame (Fig. 15c). It is remarked that simulations with subgrid chemistry modeling do not make much sense with the present non-premixed manifold, since the extinction region (for which steady non-premixed flamelets do not exist) was completed by interpolation towards the cold state. With subgrid chemistry modeling this region would be accessed frequently, either when the presumed-pdf integrations were integrated or when extinction was handled by the thickened flame model.

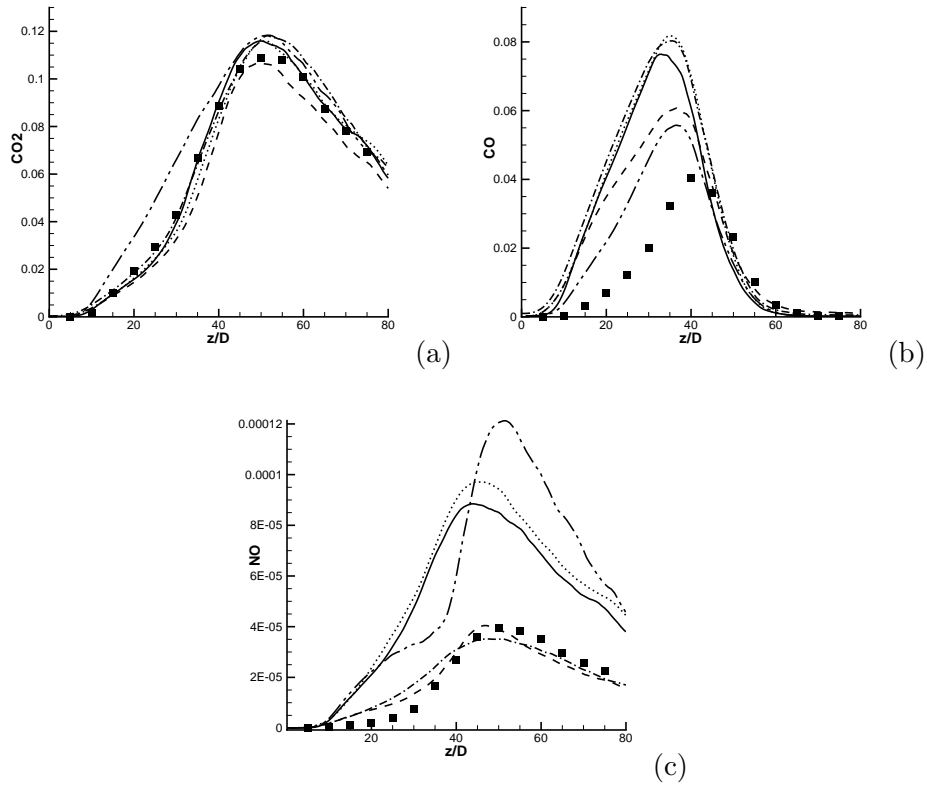


Figure 18: Flame F. Mean mass fractions of several chemical species at the centerline: CO₂ (a), CO (b) and NO (c). Four premixed simulations: without subgrid chemistry (fine grid (solid) and coarse grid (dotted)); with subgrid variance model, $b = 1$ (dash-dotted); with thickened flame model (dashed). Non-premixed simulation: without subgrid chemistry, fine grid (dash-dot-dot). The experimental data from literature [16] is denoted by square symbols.

The differences between the premixed and non-premixed simulations of flame F are more pronounced than in flame D, but otherwise tendencies are quite similar. Fig. 17-18 show the axial profiles for the temperature, main velocity and several relevant species. Fig. 18 confirms the main findings from section 4 (flame D): the prediction of CO (Fig. 18a) is lower and more accurate in the non-premixed case (for the same reason as in flame D), at the expense of the level of CO₂ (Fig. 18b). The latter profile is relatively high and less close to the experiments in the non-premixed case. The thickened flame model leads to an improvement of most profiles, because it is able to handle extinction, at least to some extent. The effect of the variances is larger than in flame D, but nevertheless small. However, there is one exception (like in flame D): the prediction of NO becomes much better when subgrid variances are included (Fig. 18c).

6 Conclusions

We compared the performances of premixed and non-premixed flamelet databases in large-eddy simulations of turbulent combustion. Since a much larger part of the reaction domain is filled by the set of steady premixed flamelets than by the set of standard non-premixed flamelets, the question was addressed whether premixed approaches are applicable to non-premixed or partially premixed flames. As test-cases the partially premixed piloted jet flames Sandia Flame D and F were simulated.

In the present LES the chemistry was parametrized by a manifold that was a function of the mixture fraction and a progress variable. Transport equations were solved for these two scalars. The inclusion of presumed β -pdf modeling of the subgrid variances of mixture fraction and progress variable was shown to have relatively small effects for both flames, unless the subgrid variances were overestimated by the model in important parts of the domain. A thickened flame model with an implicit determination of the thickening factor by estimating the sum of numerical and subgrid scalar dissipation was also tested. Due to flame thickening the scale on which extinction acts is increased, such that it can be captured by the resolved unsteady scales in the LES. Provided the wrinkling factor is tuned between lower and upper bounds taken from literature, this model was able to improve the results (of both flames) and predict significant extinction in flame F.

Premixed and non-premixed flamelet databases provided virtually the same results for the temperature, mixture fraction, and major species (except CO₂). These results were also in good agreement with the experimental data. However, the simulations overpredicted the mass fractions of CO and H₂, and the premixed case did this considerably more than the non-premixed case. To obtain suitable predictions for NO we needed to solve a transport equation for the mass fraction of NO. Without subgrid chemistry, this transport equation overpredicted the mass fractions of NO by a factor of two. However, when subgrid chemistry was taken into account, either by presumed β -pdf modeling or by thickened flame modeling, the mass fraction of NO measured in experiments was recovered within 30%.

It is concluded that when the predominantly non-premixed Sandia Flame D and F are simulated, a premixed approach is able to provide almost the same accuracy as a non-premixed approach. For steady flamelets, premixed generated manifolds cover the inequilibrium reaction region, unlike non-premixed manifolds. This property of premixed flamelets is desirable for the simulations of flames with significant inequilibrium (for example flame F).

Acknowledgement

This work is supported by the Dutch Ministry of Economic Affairs in the EET project ‘‘Greening of Gas’’ and by the Dutch Technology Foundation (STW), grant number EWO.5874.

References

- [1] H. Pitsch, *Annu. Rev. Fluid Mech.* 38 (2006), 453-482.
- [2] R.W. Bilger, S.B. Pope, K.N.C. Bray, J.F. Driscoll, *Proc. Comb. Inst.* 30 (2005), 21-42.
- [3] N. Peters, *Prog. Energy Combust. Sci.* 10 (1984), 319-339.
- [4] L. Vervisch, T. Poinso, *Annu. Rev. Fluid Mech.* 30 (1998), 655-691.
- [5] H. Pitsch, H. Steiner, *Phys. Fluids* 12 (2000), 2541-2554.
- [6] C.D. Pierce, P. Moin, *J. Fluid Mech.* 504 (2004), 73-97.
- [7] D. Bradley, L.K. Kwa, A.K.C. Lau, M. Missaghi, S.B. Chin, *Comb. Flame* 71 (1988), 109-122.
- [8] O. Gicquel, N. Darabiha, D. Thévenin, *Proc. Combust. Inst.* 28 (2000), 1901-1908.
- [9] J.A. van Oijen, F.A. Lammers, L.P.H. de Goey, *Comb. Flame* 127 (2001) 2124-2134.
- [10] J.A. van Oijen, L.P.H. de Goey, *Combust. Theory Modelling* 6 (2002), 463-478.
- [11] J.A. van Oijen, PhD. Thesis, TU Eindhoven (2002).
- [12] D. Bradley, P.H. Gaskell, X.J. Gu, *Proc. Combust. Inst.* 27 (1998) 1199-1206.
- [13] B. Fiorina, O. Gicquel, L. Vervisch, S. Carpentier, N. Darabiha, *Comb. Flame* 140 (2005) 147-160.
- [14] H. Bongers, J.A. van Oijen, L.M.T. Somers, L.P.H. de Goey, *Combust. Sci. and Tech.* 177 (2005) 2373-2393.
- [15] D. Bradley, D.R. Emerson, P.H. Gaskell, X.J. Gu, *Proc. Combust. Inst.* 29 (2002), 2155-2162.
- [16] R.S. Barlow, J.H. Frank, *Proc. Combust. Inst.* 27 (1998) 1087-1095 (experimental database at www.ca.sandia.gov/TNF/DataArch/FlameD.html).
- [17] W. Meier, R.S. Barlow, Y.-L. Chen, J.-Y. Chen, *Comb. Flame* (2000), 326-343.
- [18] C. Schneider, A. Dreizler, J. Janicka, E. Hassel, *Comb. Flame* 135 (2003) 185-190.
- [19] A.M. Kempf, PhD-Thesis, TU Darmstadt (2003).
- [20] G.M. Goldin, *AIAA Paper* 2005-555 (2005), 1-13.
- [21] C. Geiss, Diplomarbeit, TU Darmstadt (2005).
- [22] B.A. Albrecht, W.J.S. Ramaekers, J.A. van Oijen, R.J.M. Bastiaans, L.P.H. de Goey, submitted (2007).
- [23] R.R. Cao, S.B. Pope, *Comb. Flame* 143 (2005), 450-470.
- [24] M.R.H. Sheikhi, T.G. Drozda, P. Givi, F.A. Jaber, S.B. Pope, *Proc. Comb. Inst.* 30 (2005), 549-556.
- [25] R. Mustata, L. Valino, C. Jimenez, W.P. Jones, S. Bondi, *Comb. Flame* 145 (2006), 88-104.
- [26] R.R. Cao, H. Wang, S.B. Pope, *Proc. Comb. Inst.* 31 (2007), 1543-1550.
- [27] R.S. Barlow, J.H. Frank, A.N. Karpetis, J.-Y. Chen, *Comb. Flame* 143 (2005), 433-449.

- [28] M.D. Smooke, V. Giovangigli, In 'Reduced kinetic mechanisms and asymptotic approximations for methane-air flames', ed. M.D. Smooke, Springer Verlag Berlin (1991), 1-28.
- [29] A.W. Vreman, Phys. Fluids 16 (2004), 3670-3681.
- [30] A. Leonard, Adv. Geophys. 18 (1974), 237.
- [31] R.A. Clark, J.H. Ferziger, W.C. Reynolds, J. Fluid Mech. 91 (1979), 1-16.
- [32] M. Germano, U. Piomelli, P. Moin, W. Cabot, Phys. Fluids A 3 (1991), 1760-1765.
- [33] F. Nicoud, F. Ducros, Flow, Turbulence and Combustion 62 (1999), 183-200.
- [34] O. Colin, F. Ducros, D. Veynante, T. Poinso, Phys. Fluids 12 (2000), 1843-1863.
- [35] G.P. Smith, D.M. Golden, M. Frenklach, N.W. Moriarty, B. Eiteneer, M. Goldenberg, C.T. Bowman, R.K. Hanson, S Song, W.C. Gardiner Jr., V.V. Lissianski, Z. Qin, http://www.me.berkeley.edu/gri_mech/
- [36] A.W. Cook, J.J. Riley, Phys. Fluids 6 (1994), 2868-2870.
- [37] C. Wall, B.J. Boersma, P. Moin, Phys. Fluids 12 (2000), 2522-2529.
- [38] P.J. O'Rourke, F.V. Bracco, J. Comp. Phys. 33 (1979) 185-203.
- [39] F. Charlette, C. Meneveau, D. Veynante, Comb. Flame 131 (2002) 159-180.
- [40] C. Meneveau, T. Poinso, Comb. Flame 86 (1991), 311-332.
- [41] F.C. Gouldin, Comb. Flame 68 (1987), 249-266.
- [42] J.P. Legier, T. Poinso, D.V. Veynante, CTR Proceedings Summer Program 2000.
- [43] B. Merci, E. Dick, J. Vierendeels, C. de Langhe, Int. J. Heat Fluid Flow 12 (2002), 65-80.
- [44] A.W. Vreman, Phys. Fluids 16 (2004), 2012-2022.
- [45] P.E. DesJardin, S.H. Frankel, Phys. Fluids 10 (1998), 2298-2314.
- [46] N. Branley, W.P. Jones, Comb. Flame 127 (2001), 1914-1934.
- [47] N. Peters, Turbulent Combustion, Cambridge (2000).